

## JGR Solid Earth

## RESEARCH ARTICLE

10.1029/2019JB018675

## Key Points:

- Video-derived sea level time histories are critical to accurately model the inundation and to identify the dominant tsunami sources in Palu
- Earthquake source modeling using InSAR data shows that coseismic deformation played only a minor role in generating the 2018 Palu tsunami
- Tsunami inversions using video-derived time histories show that a few landslides in Palu Bay were the major contributors to the tsunami

## Supporting Information:

- Supporting Information S1

## Correspondence to:

I. Sepúlveda,  
sepulveda@ucsd.edu

## Citation:

Sepúlveda, I., Haase, J. S., Carvajal, M., Xu, X., & Liu, P. L. F. (2020). Modeling the sources of the 2018 Palu, Indonesia, tsunami using videos from social media. *Journal of Geophysical Research: Solid Earth*, 125, e2019JB018675. <https://doi.org/10.1029/2019JB018675>

Received 11 SEP 2019

Accepted 17 FEB 2020

Accepted article online 19 FEB 2020

## Modeling the Sources of the 2018 Palu, Indonesia, Tsunami Using Videos From Social Media

Ignacio Sepúlveda<sup>1</sup> , Jennifer S. Haase<sup>1</sup> , Matias Carvajal<sup>2,3</sup> , Xiaohua Xu<sup>1</sup> , and Philip L. F. Liu<sup>4,5,6</sup>

<sup>1</sup>Cecil H. and Ida M. Green Institute of Geophysics and Planetary Physics, Scripps Institution of Oceanography, University of California, San Diego, CA, USA, <sup>2</sup>Escuela de Ciencias del Mar, Pontificia Universidad Católica de Valparaíso, Valparaíso, Chile, <sup>3</sup>Millennium Nucleus The Seismic Cycle Along Subduction Zones, Chile, <sup>4</sup>Department of Civil and Environmental Engineering, National University of Singapore, Singapore, <sup>5</sup>School of Civil and Environmental Engineering, Cornell University, Ithaca, NY, USA, <sup>6</sup>Institute of Hydrological and Oceanic Sciences, National Central University, Jhongli, Taiwan

**Abstract** The 2018 Palu tsunami contributed significantly to the devastation caused by the associated  $M_w$  7.5 earthquake. This began a debate about how the moderate size earthquake triggered such a large tsunami within Palu Bay, with runups of more than 10 m. The possibility of a large component of vertical coseismic deformation and submarine landslides have been considered as potential explanations. However, scarce instrumental data have made it difficult to resolve the potential contributions from either type of source. We use tsunami waveforms derived from social media videos in Palu Bay to model the possible sources of the tsunami. We invert InSAR data with different fault geometries and use the resulting seafloor displacements to simulate tsunamis. The coseismic sources alone cannot match both the video-derived time histories and surveyed runups. Then we conduct a tsunami source inversion using the video-derived time histories and a tide gauge record as inputs. We specify hypothetical landslide locations and solve for initial tsunami elevation. Our results, validated with surveyed runups, show that a limited number of landslides in southern Palu Bay are sufficient to explain the tsunami data. The Palu tsunami highlights the difficulty in accurately capturing with tide gauges the amplitude and timing of short period waves that can have large impacts at the coast. The proximity of landslides to locations of high fault slip also suggests that tsunami hazard assessment in strike-slip environments should include triggered landslides, especially for locations where the coastline morphology is strongly linked to fault geometry.

## 1. Introduction

The 28 September 2018  $M_w$  7.5 strike-slip earthquake that struck Sulawesi Island, Indonesia, was followed by an unexpectedly large tsunami, which significantly contributed to the casualties and property loss associated with the earthquake (Muhari et al., 2018). The impact of the tsunami was particularly significant at the southern end of Palu Bay, where >5 m height tsunami waves arrived a few minutes after the ground shaking stopped (Carvajal et al., 2019). A debate within the scientific community immediately ensued about the mechanism for generating such a large tsunami following a predominantly strike-slip earthquake. Two possible explanations are that either the complexity of the fault structure hidden beneath the bay included a significant component of dip-slip motion to produce the vertical uplift necessary to generate the tsunami or that one or multiple submarine landslides triggered by the earthquake were the main cause. The particular coastline geometry and bathymetry at Palu are conducive to focusing tsunami energy, as a direct result of the tectonic setting, which can be seen in Figure 1a. The relief follows the geologically mapped Palu-Koro fault (Bellier et al., 2001; Watkinson & Hall, 2017), a major transform fault at the boundary of the Sula block, connecting the Minahassa Trench to the north with the Makassar Trench to the west. The rapid deformation rate of 42 mm/year (Socquet et al., 2006) (mostly strike-slip) creates steep topography, and the high sediment load from rivers flowing into the bay creates subsurface slopes that are susceptible to landslides (Sassa & Takagawa, 2019). Secondary faults on the east side of the bay identified by GPS velocity transects (Socquet et al., 2006) also define the geometry of the narrow bay and contribute to the hazard. Historical tsunamis comparable to the 2018 event have been associated with significant earthquakes in 1927, 1938, 1968, and 1996 (Pelinovsky et al., 1997; Prasetya et al., 2001), with varying strike-slip, normal and thrust mechanisms, attributed to the complexity of the tectonic setting.

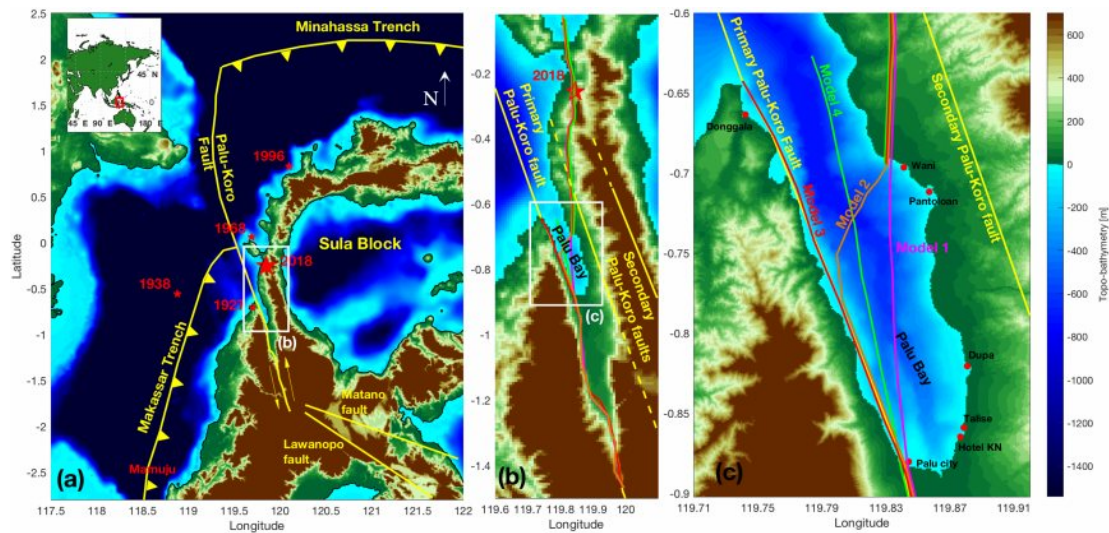


**Figure 1.** (a) Regional map with major plate boundary faults of the Sula Block. Historical earthquakes associated with tsunamis in the last century are indicated with a star and year. (b) Map of Palu Bay and the locations of the main Palu-Koro fault and parallel secondary faults identified on the east side of Palu Bay from a GPS velocity transect (Socquet et al., 2006) (yellow, dashed where assumed). Four fault geometries are proposed in this study, and their corresponding fault traces are shown in magenta, orange, red, and green. (c) Enlargement of Palu Bay showing the differences of the proposed fault geometries beneath the bay. Model 1 (magenta) has a straight fault trace beneath the bay, connecting the fault trace observed at Palu City (Lon. 119.828° Lat.  $-0.690^\circ$ ) to a point close to Pantoloan (Lon. 119.842° Lat.  $-0.883^\circ$ ). Model 2 (orange) assumes the same geometry on land as Model 1 but follows the Palu-Koro fault along the coast and then makes a restraining bend in the middle of the bay. Model 3 (red) follows the main geologic trace of the Palu-Koro fault and then jumps to the observed northeastern fault trace. Model 4 (green) assumes a fault approximately aligned with the trough in the bathymetry along the central axis of the bay. The locations of Palu City, Talise, Hotel KN, Dupu, Pantoloan port, Wani, and Donggala are also shown. Tide gauges are located at Mamuju (to the south in panel a) and Pantoloan (west coast in panel c).

The rapid teleseismic earthquake source inversion by the USGS (referred to as the USGS model hereafter) produced a fault rupture that initiated  $\sim 30$  km northeast of the geologically mapped Palu-Koro fault and cut across the general orientation of the bay. A single straight fault with the same orientation was also used in a joint inversion for the fault slip constrained with InSAR and optical imagery data (Socquet et al., 2019). These results and slip models from other researchers have been used to estimate the coseismic seafloor deformation and the corresponding initial tsunami surface elevation (e.g., Heidarzadeh et al., 2019) however, the tsunami simulations underestimate the runup heights reported in the post-tsunami surveys (Fritz et al., 2018; Omira et al., 2019). As a result, the exact geometry of the faults beneath the bay became critically important to understanding the tsunami source mechanism. At the tide gauge station in Pantoloan, the tide records in the hours before and after the tsunami show that the mean sea level did not change as a result of the earthquake (see top right panel of Figure 2), eliminating the possibility of a large amount of deep dip slip. Post-tsunami surveys also have not shown evidence of significant permanent changes in relative sea level, except for areas of very localized coastal collapse likely linked to landslides (e.g., Muhari et al., 2018; Sassa & Takagawa, 2019).

The difficulties in reproducing the observed tsunami runup heights and the Pantoloan tide gauge record have led to the alternative hypothesis of landslide sources. There is ample evidence that extensive landslides occurred along the coast of Palu Bay. Takagi et al. (2019), for instance, conducted near shore topographic and bathymetric surveys in the southwestern section of Palu Bay. They found evidence of a significant landslide with an area of  $\sim 1$  km<sup>2</sup>, which may be related to the generation of tsunami waves, as reported by eye-witnesses. Sassa and Takagawa (2019) conducted a survey along the coast of the bay and found evidence of liquefaction-induced coastal collapse and associated local subsidence that could have generated tsunami waves as a result of liquefied sediment flows. Carvajal et al. (2019) detected areas of coastal collapse and tsunamigenic potential by analyzing satellite imagery from Google Earth and by collecting social media videos from nearby locations showing the generation of tsunami waves.

More complex coseismic deformation models have been developed in an effort to reproduce the specific details of the tsunami (e.g., Ulrich et al., 2019; Yolsal-Çevikbilen & Taymaz, 2019) and to combine landslide and coseismic sources (e.g., Gusman et al., 2019). However, the tide gauge at Pantoloan port and

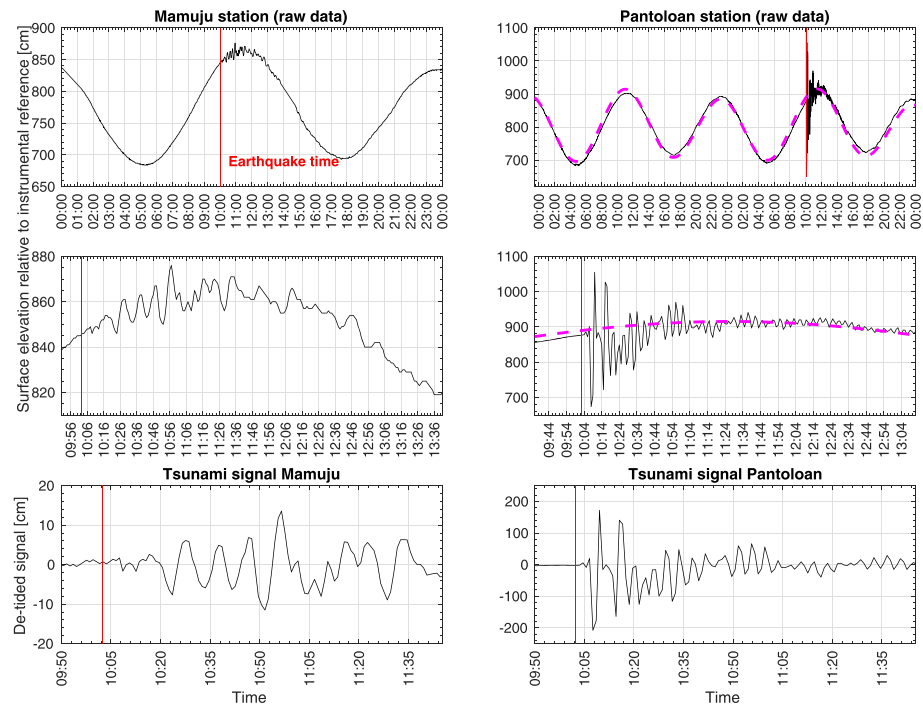


**Figure 2.** Tsunami records for Pantoloan and Mamuju stations. The top row shows the measured sea level surface elevation over one day in Mamuju and over two days in Pantoloan port. The second row enlarges the data around the time of the tsunami. The third row shows the tsunami signals after removing tides and the mean. The magenta dashed curve corresponds to a tidal prediction based on tidal records in October and November of 2018 (60 days).

the post-tsunami surveys measuring the runup heights (e.g., Fritz et al., 2018; Omira et al., 2019) which are used to characterize the tsunami do not uniquely constrain the source. The quantitative evidence presented to date is insufficient to definitively prove or disprove the existence and relative contribution of earthquake-generated seafloor deformation versus landslides as the source of the tsunami waves. Hence, a study utilizing new complementary information of the tsunami and the earthquake would provide crucial insights.

In this work we test the hypothesized contributions to the tsunami from coseismic deformation and multiple landslide sources, taking advantage of a unique compilation of 43 crowdsourced social media videos (Carvajal et al., 2019). Some were smart phone videos taken by individuals and some were closed circuit television (CCTV) videos. These videos were all posted to social media accounts, such as Twitter and YouTube, and were thus accessible for citizen science. Each video location and orientation was identified by feature matching in Google maps. Time histories of surface elevations were constructed by consecutive tracking of water level in timed video frames relative to the initial still water level. Absolute timing of tsunami arrivals was possible for a subset of the videos that captured both the seismic shaking and the tsunami waves or inundation, the others have only relative timing. These video-derived time histories are valuable additional data for evaluating the hypothetical tsunami sources. The archive of videos and derived time histories can be accessed at <https://agsweb.ucsd.edu/tsunami/> (Carvajal et al., 2019). Tsunami witness videos shared via social media have been used in past studies of the 2004 Indonesia and 2011 Japan tsunamis. Fritz et al. (2006) and Fritz et al. (2012) resurveyed the locations of survivor videos with LiDAR technology and used particle image velocimetry techniques to infer wave amplitudes and flow speeds in coastal areas of Banda Aceh, Indonesia, and Kesennnuma Bay, Japan. Lynett et al. (2012) used videos to estimate current speeds and dimensions of eddies in Port of Oarai, Japan, during the 2011 tsunami. These estimates were employed to qualitatively evaluate numerical tsunami simulations. In contrast, our study uses the video-derived data as pseudo-observations in the place of tide gauges to assess the accuracy of the simulation results and serve as input to the numerical tsunami source inversion. We essentially exploit the data derived from citizen science to increase the observational network, with appropriately assigned errors.

The available tide gauge records in the region are analyzed in section 2 to provide first order constraints on source locations. To test the hypothesis that the tsunami was generated by coseismic deformation, in section 3, we carry out a suite of finite fault slip inversions from InSAR data. We assess the sensitivity to the fault geometry beneath the bay by using 12 hypothetical geometries which produce different coseismic deformation fields. They are then used to simulate the tsunami generation and propagation within the bay, and the inundation in terms of the tsunami runup height. For the hypothesis that the tsunami was generated by landslides, in section 4, we conduct an inversion for the initial tsunami surface elevation using the video-derived time histories at six locations within Palu Bay (Carvajal et al., 2019) as input data. We assume a limited number of tsunami sources located within the bay based on the short observed travel times and solve for the amplitude of the initial tsunami surface elevation at each source. In both sections, we use surveyed tsunami runup heights and the fit to the digitized video-derived time histories of the tsunami surface elevation as key data sets to test the hypotheses. In section 5, we evaluate the sensitivity of the results to uncertainties in the video-derived data timing, amplitude and location, and uncertainties in the assumed landslide source locations.

## 2. Analysis of Tide Gauge Records in Mamuju and Pantoloan

Tide gauge records at Mamuju and Pantoloan (see Figure 1) were provided by the Badan Informasi Geospasial (BIG) and are shown in Figure 2. The first row of Figure 2 shows the raw data, the second row shows an enlargement of the period around the tsunami, and the third row shows the signals after removing the tides. For the de-tiding process, we employed the harmonic analysis of the t-tide toolbox available for Matlab (Pawlowicz et al., 2002). The dashed magenta curve on the Pantoloan record is the resulting tide estimation without tsunami based on the tide record for the period of October and November 2018 (60 days). The prediction has an accuracy of  $\pm 15$  cm. The magenta curve shows that no vertical coseismic deformation occurred at Pantoloan.

Reverse wave tracing from the Pantoloan tide gauge location to the time of the earthquake constrains the tsunami source to be within Palu Bay (Carvajal et al., 2019). Reverse wave tracing from Mamuju station, in contrast, shows that the furthest north and closest that the source of the waves seen in this record could be to Palu Bay is approximately 100 km south of the entrance to the bay. This is not consistent with the source producing the wave arrival time at Pantoloan, and therefore, it must be generated outside Palu Bay by a secondary source. We can make no interpretation about the nature of this secondary source, but given that there were no large immediate aftershocks near that location, the most likely explanation is ground failure or landslide. Furthermore, the reverse wave tracing analysis shows that such a source north of Mamuju would need  $\sim 28$  min to reach the entrance to Palu Bay. Any possible interaction of these smaller waves from such a source would occur well after the first 15 min of high amplitude tsunami waves at Pantoloan that are the subject of this investigation. Therefore, we exclude the Mamuju record from the analysis in this paper. Details supporting the timing of the tide gauge records and reverse wave tracing are presented in supporting information Figure S1.

BIG clarified that sea level at the Pantoloan tide gauge station is measured using three independent sensors. However, the tsunami was continuously measured throughout the duration of the tsunami only by the acoustic Doppler-based sensor located inside the port basin. Instrument samples made at 1 s interval are averaged over 30 s, which low pass filters the signal, then they are decimated to 1 min. This is a relevant limitation for capturing tsunami waves with periods shorter than 2 min.

## 3. Earthquake Generated Tsunamis

It is well known that the sudden deformation of the seafloor during an earthquake perturbs the still water level and generates a tsunami wave due to the restoration of sea level by gravitational forces. The generation mechanism is primarily due to the coseismic vertical seafloor deformation. However, the horizontal seafloor displacements may also contribute to this perturbation when the seafloor has a steep slope (Tanioka & Satake, 1996). The magnitude and orientation of the slip (e.g., the relative contributions in the dip slip or strike slip directions) and fault geometry play a primary role defining the coseismic seafloor deformation. The available InSAR data on land are used here to invert for the earthquake slip using several plausible fault geometries beneath the bay, from which we simulate the resulting tsunami.



### 3.1. Earthquake Models Based on Inversion of Coseismic Displacement Data

We create four alternative fault geometries to assess the impact of the uncertainty of the fault trace on the inverted slip distribution and the simulated tsunamis. The earthquake models share the same geometry on land on the northeastern side of Palu Bay and south of Palu City, where the InSAR data determine the fault trace, but differ beneath the bay (see Figure 1c). In constructing the hypothetical fault geometries, we consider the location of the primary Palu-Koro fault trace along the steep western coastline of Palu Bay (Prasetya et al., 2001) and the identified secondary faults (Socquet et al., 2006) to the east of the bay (see Figure 1b). Model 1 (magenta) has a continuous straight fault trace beneath the bay, connecting the fault trace observed at Palu City (Lon. 119.828353° Lat.  $-0.690768^\circ$ ) to a point northwest of Pantoloan port (Lon. 119.842516° Lat.  $-0.883752^\circ$ ) where the InSAR derived fault trace intersects the coastline. The geometry of Model 1 is similar to that proposed by Socquet et al. (2019) and the USGS model. Model 2 (orange) is based on the recent maps of active faults (Watkinson & Hall, 2017) that show the main trace of the Palu-Koro fault along the coastline on the west side of the bay and a minor parallel fault trace on the east side of the bay. Model 2 carries the fault rupture along that main trace then jumps to the eastern trace, creating a restraining bend beneath the middle of the bay. Models 3 (red) and 4 (green) are constructed with fault discontinuities beneath Palu Bay, which would also generate compressional vertical deformation for a left lateral strike-slip fault mechanism. Model 3 has one segment following the main Palu-Koro fault along the west side of the bay as in Watkinson and Hall (2017). Since there are no direct signs of a fault trace in the bay bathymetry, this geometry would appear to be equally likely as Model 2. Model 4, on the other hand, assumes the primary fault is roughly aligned with the submarine canyon along the central axis of the bay at the point where the rupture goes offshore, as seen in the InSAR data 3. There are no specific observations to support Model 4 other than the large scale bathymetry, and it is included in order to represent an intermediate value of the fault plane strike. The dip angle is varied to be  $70^\circ$ ,  $80^\circ$ , and  $89^\circ$  for each fault trace, creating 12 fault models.

The static slip inversion is constrained with InSAR data acquired by the Advanced Land Observing Satellite-2 (ALOS-2) satellite in Scansar mode, operated by the Japanese Aerospace Exploration Agency (JAXA). We employed three observations, from one ascending and two descending satellite tracks. The time offset between the satellite passes is shown at the top of Figure 3a. Three observations were used to determine three interferograms aligned with the line of sight (LOS), and two are utilized to determine interferograms along the track direction, as shown in Figure 3a. The line of sight (LOS) of the InSAR data is nearly east-west, which is perpendicular to the predominantly north-south strike-slip fault motion. As a consequence, the component of LOS displacement observed in the north-south direction is small, with high relative uncertainties. This may lead to high uncertainties in the resulting slip models. Thus, along-track oriented interferograms are included in the inversion, which have much larger north-south components of motion.

The data were processed with the GMTSAR software (Sandwell et al., 2011), with additional post processing using GMT (Wessel et al., 2013) and phase unwrapping using SNAPHU (Chen & Zebker, 2001). The deformation field recovery by phase unwrapping is very challenging for the Palu earthquake mainly due to radar decorrelation near the fault trace and across the open water of Palu Bay. Thus we first perform multi-aperture interferometry (MAI) on the SAR data and determine the fault trace from the maximum decorrelation within the fault zone and the location of the fault offset from the optical imagery from Sentinel-2. Then, we divide the interferogram into several blocks of well-correlated regions, unwrap them individually, and assemble them back to one full deformation map taking advantage of overlapping regions of strong phase correlation. Unwrapping this way reconstructs continuous phase around the ends of the fault to acquire a better estimate of the large scale deformation field. A trend is estimated using far field interferogram data and removed in both the MAI and unwrapped phase in order to mitigate ionospheric effects and potential coregistration errors. The resulting unwrapped deformation fields calculated from the interferograms are low-pass filtered below 0.9 km to remove high wave number noise which may be associated with artifacts (e.g., decorrelation) and indirect tectonic processes such as landslides. We also remove data which are close to the observed surface fault trace where the phase is not coherent due to motions larger than one cycle. To mitigate residual effects of removing the trend, a linear ramp term for one of the along track interferograms is estimated and removed in the inversion. This residual nonphysical trend might be attributed to remaining coregistration and ionospheric errors (Simons et al., 2002).

The model fault trace is extended from the surface to a depth of 25 km and discretized into subfaults of  $2.5 \text{ km} \times 2.5 \text{ km}$  size. In total, the subfaults cover a length of  $\sim 200 \text{ km}$ . The unknown parameters are the dip-slip and strike-slip components of slip on each of the subfaults and the coefficients of the linear ramp

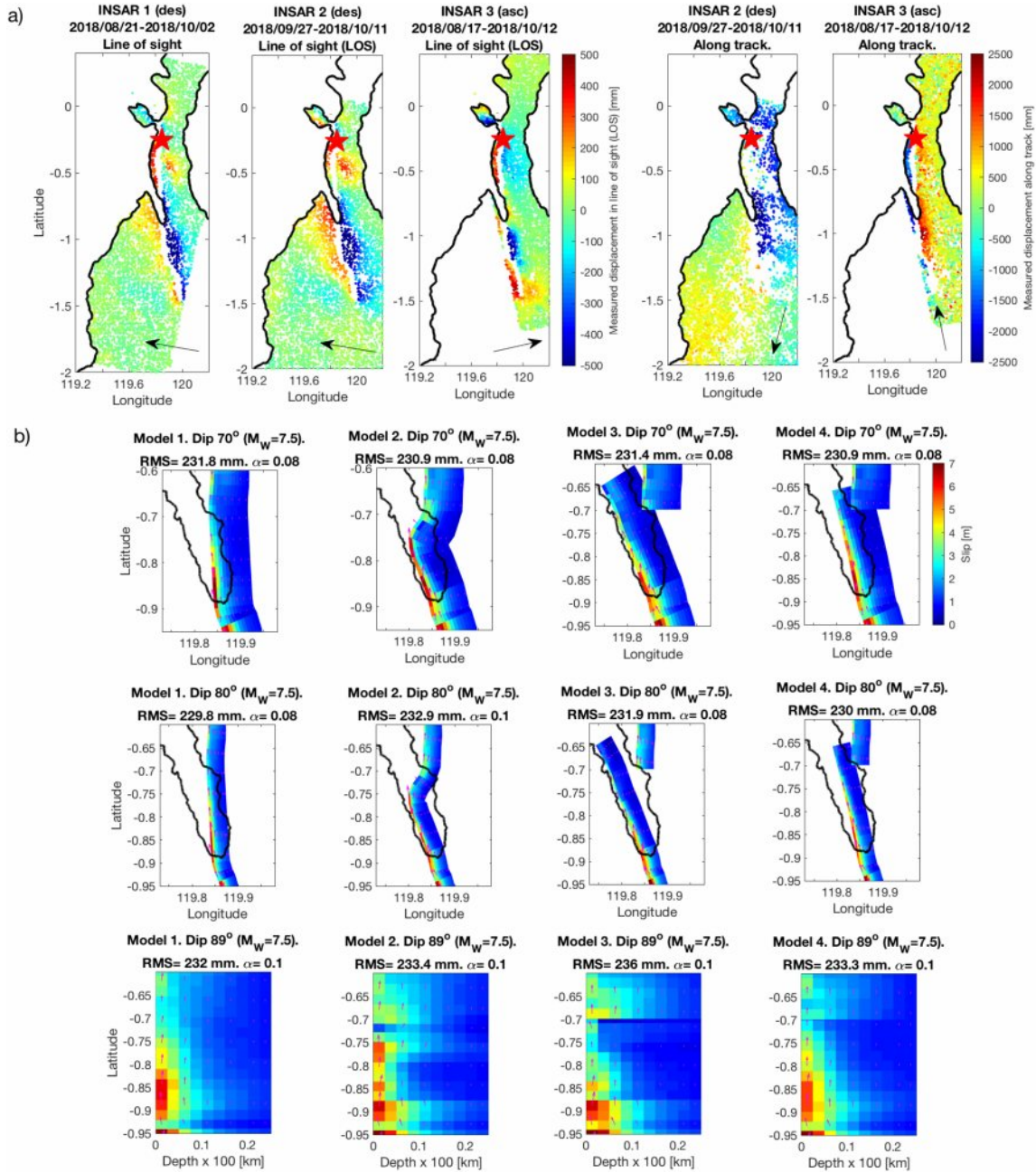


**Figure 3.** (a) InSAR data sets used in the slip inversions from ALOS-2 descending (1 and 2) and ascending (3) passes. Three interferograms are determined with an orientation in the line of sight (LOS), and two are determined with an orientation along-track. Positive values indicate displacements away from the satellite for LOS data and displacement oriented toward the satellite azimuth for the along-track data. The dates of the observations are shown in the headers. The horizontal projections of the LOS and the along-track directions are shown by black arrows. The red star indicates the USGS estimated epicenter of the 2018 Sulawesi earthquake, and the black curve shows the coastline of Sulawesi. (b) Static slip models of the 2018 Sulawesi earthquake using four different assumed fault trace geometries. The dip angles associated with each fault trace model was varied from 70°, 80°, and 89°, resulting in a total of 12 slip models. The color indicates the total slip magnitude, and the magenta arrows indicate the rake. The RMS errors of each inversion are shown in the header of the figures.

for one of the along-track InSAR data sets. The ramp has the form  $c_1x + c_2y + c_3 = z$ , where  $x$ ,  $y$ , and  $z$  are the point locations within the image and  $c = (c_1, c_2, c_3)$  are the ramp coefficients. The static slip inversion uses regularized least squares to solve the system of equations

$$As + Rc = d, \quad (1)$$

where  $A$  is the matrix of Green functions relating fault slip to observed surface displacement for a homogeneous half space (Okada, 1985),  $d$  corresponds to the InSAR data vector having 4,000 values per data set

(20,000 in total),  $s$  corresponds to the unknown slip values, and  $R$  is a matrix containing three columns for the values of  $x$ ,  $y$ , and 1. Matrices  $A$  and  $R$  are concatenated into a single matrix,  $B$ , and the vectors  $s$  and  $c$  are concatenated into the vector of unknowns,  $u$ .

$$Bu = d. \quad (2)$$

A Tikhonov regularization is employed for numerical stability,

$$u = (B^*B + \alpha I)^{-1} B^* d, \quad (3)$$

where  $\alpha$  is the Tikhonov regularization parameter and  $I$  is the identity matrix. The five InSAR data sets (i.e., three in LOS and two along track) are weighted equally. Values of  $\alpha$  are varied between 0.08 and 0.2, to find the smoothest model which has a magnitude of  $M_w$  7.5, assuming a shear modulus of 30 GPa. The resulting slip distributions beneath Palu Bay are shown in Figure 3b. The entire fault with all the estimated subfaults for the 12 earthquake models are shown in Figures S2 and S3. Figures S4–S15 also present the inversion errors.

The largest slip beneath the bay found for any model is less than 8 m and is predominantly strike-slip and concentrated south of latitude  $-0.75^\circ$ . Model 2 is associated with a strong dip-slip component of  $\sim 3$  m at the hypothetical fault bend, which gives it a larger tsunamigenic potential than the other models. The resulting RMS errors of the 12 slip models are very similar, so it is not possible to judge which model is the best based on the fit to the InSAR observations. The teleseismic source inversions from the USGS showed that the seismic data can also be fitted with a model with less than  $\sim 2$  m of dip-slip component. This model and the model of Socquet et al. (2019), determined from optical image correlation data, give a range of small dip-slip components that will also be evaluated in the tsunami simulations.

The accuracy of the slip inversions depends on the distance between the data and the modeled subfaults. The InSAR data extend along the entire length of the fault. However, it is the slip beneath the bay that is of most interest for the tsunami modeling. In this region, the observations on land can be as much as  $\sim 5$  km from the hypothetical fault traces. We include a sensitivity analysis in the supporting information to show that deep subfaults beneath the bay are not constrained as well by ground displacements (see Figure S16), and deep dip slip cannot be excluded on the basis of the inversion. However, at the tide gauge station in Pantoloan, the tide records before and after the tsunami show that the mean sea level did not change during the earthquake, eliminating the possibility of a large amount of deep dip slip (see magenta curve in Figure 2). Post-tsunami surveys also have not shown evidence of significant permanent changes in relative sea level as a direct consequence of the earthquake coseismic deformation. New bathymetric and subsurface geological surveys covering the entire bay would be useful to determine whether there is any evidence of fault rupture or evidence of fault-related seafloor deformation patterns beneath the bay.

The slip models of this section used Green functions based on the Okada model which assumes a homogeneous half space, as commonly used in tsunami studies. More complex models can be adopted, for example, considering layered rigidity of the crust. However, even if they produce more slip on the fault plane, the surface deformation on land would likely be similar in order to fit the data. Furthermore, there is not enough information to constrain heterogeneous rigidity beneath the bay.

There is evidence that the 2018 earthquake rupture was characterized by supershear rupture velocities (Bao et al., 2019; Mai, 2019; Socquet et al., 2019). Kinematic properties of the earthquake, however, are suggested to be relevant for tsunami generation only when rise times are long and rupture velocities are low (Fuentes et al., 2018). Thus, uncertainties in the kinematic properties of the rupture are expected to produce little impact on the simulation of tsunamis at Palu Bay.

All the inverted slip models show large slips at the south end of Palu Bay (Figure 4b), and south of Palu City where they are continued about 120 km further south (see Figures S2 and S3 for the slip model for the entire length of the fault). The high slip south of Palu City is well constrained by the significant coseismic InSAR displacements seen in Figure 4a. Other slip models (e.g., Socquet et al., 2019, shown in Figure S17), also predict high strike slip in this location. We have examined the trade-off with regularization parameters and determined that the slip values in the inversions are robust and are present in all model results. We selected the regularization parameters which generate earthquakes with a magnitude  $M_w$  7.5, so contain the minimum roughness required to satisfy that constraint. These large slip values near the south end of Palu Bay are important features for the resulting tsunami simulations.



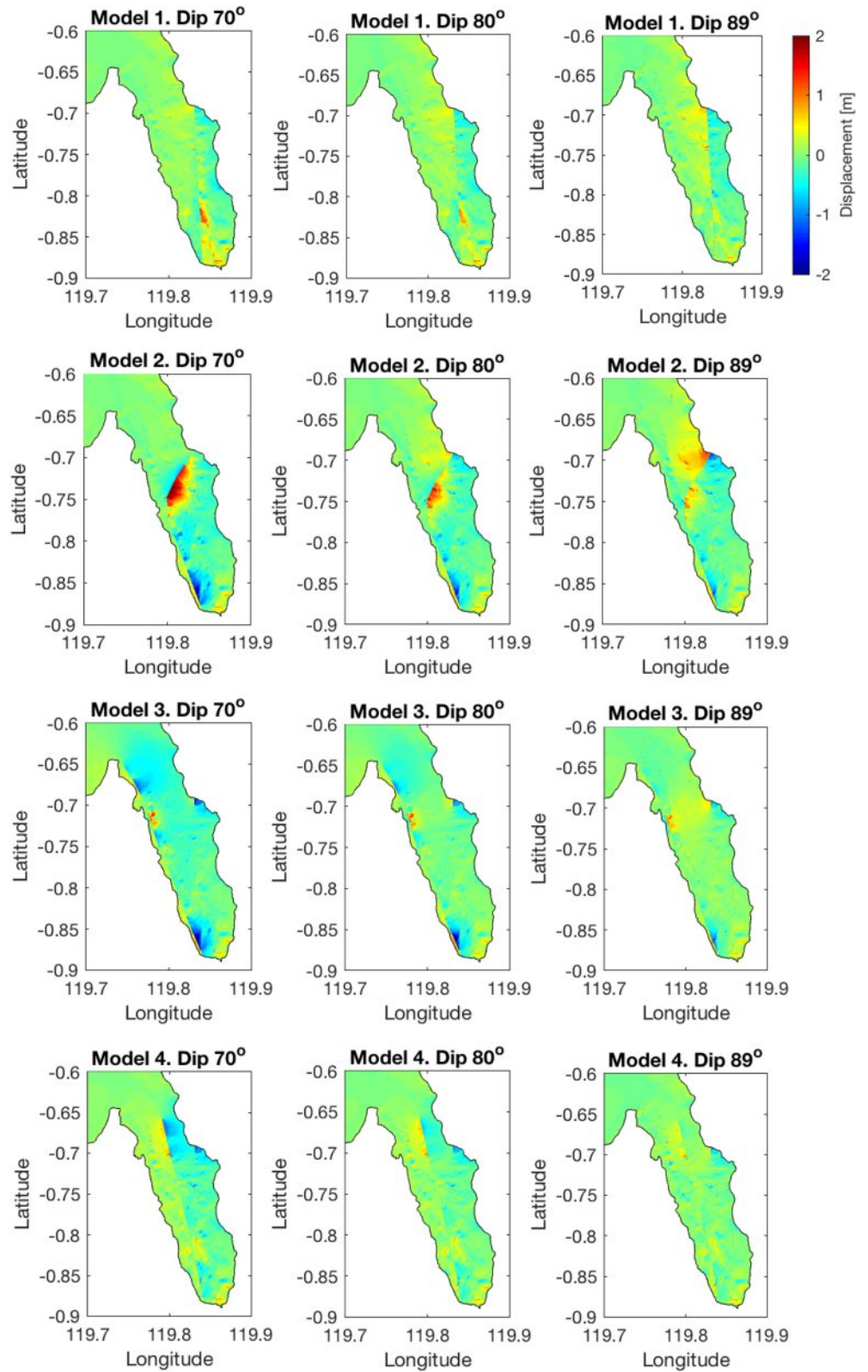


**Figure 4.** Initial tsunami surface elevations corresponding to the 12 slip distributions analyzed in this study. The initial surface elevation, represented as displacement from the still water level, includes the contribution of the static vertical and horizontal coseismic deformation.



### 3.2. Simulation of Tsunamis Generated by Coseismic Deformation

The slip distribution models obtained in the previous section are employed to simulate the tsunami propagation and inundation. As explained in section 2, the timing of the tsunami waves limits the sources and most relevant tsunami responses to within the bay. Hence, the tsunami model domain is defined by the size of the bay.

The initial tsunami surface elevations are obtained by using a model of the seafloor deformation (Okada, 1985) based on the slip results from the static slip inversions. We consider the superposition of the vertical ( $\eta_z^0$ ) and horizontal ( $\eta_h^0$ ) contributions. The vertical contribution is assumed to be equivalent to the vertical coseismic displacement at the seafloor. The horizontal contribution can be expressed as (Tanioka & Satake, 1996)

$$\eta_h^0 = u_x \frac{\partial H}{\partial x} + u_y \frac{\partial H}{\partial y}, \quad (4)$$

where  $u_x$  and  $u_y$  are the horizontal coseismic deformation in the  $x$  and  $y$  directions, respectively, and  $H$  is the water depth. Note that the horizontal contribution is only relevant when horizontal displacements are large and seafloor slopes are steep. The modeled initial tsunami surface elevations are shown in Figure 4. Among the models analyzed, Model 2 with dip angle  $70^\circ$  is associated with the largest earthquake coseismic deformation contribution to the tsunami generation.

Figure 4 shows small amplitude short wavelength variations in the initial water surface elevation due to similar scale variations in the seafloor coseismic deformation. These are unrealistic, because sharp patterns of vertical seafloor deformation cannot be transmitted to the water surface elevation if their wavelengths are comparable to the water depth (i.e., wavelengths  $< 3$  times the water depth) (Kajiura, 1963). However, these are small and will have a low impact on the simulation of the longer wavelength content of the tsunami waves. The approach of Tanioka and Satake (1996) to include the effect of horizontal coseismic deformation also relies on the assumption that the horizontal scales are larger than the water depth, so that shallow wave theory holds. To some extent, the short wavelength patterns in the initial sea surface elevation could be due to the inaccuracies of including short wavelength horizontal motions, but these would also have a small impact. Furthermore, the approach does not consider dynamic contributions from the seafloor movement; in particular, mass is conserved, but the injection of momentum from the horizontal seafloor motion is ignored. While existing studies show that momentum is indeed transmitted to the oceans by the horizontal coseismic deformation (Song et al., 2008; 2017), this is mostly carried away by ocean acoustic waves rather than tsunami waves (Lotto et al., 2017).

The tsunami model is configured using a single numerical grid with resolution of  $\sim 45$  m and solved with a time step of 1 s to comply with the Courant criterion (Wang, 2009). Simulations in Figure S19 demonstrate that simulated runup heights are similar when 45 m or finer resolutions are adopted. The contoured bathymetry and topography provided by the Geospatial Information Agency of Indonesia (BIG) from a survey in 2014 is interpolated to this grid for the entire bay. A higher resolution data set from 2015 is available, but it covers a smaller area and contains some evident errors. For example, it has shallow depths at the entrance of the bay, which are not seen in newer data sets (e.g., Frederik et al., 2019), so we disregard the 2015 survey in our analysis.

We apply a correction to refer the bathymetry to the mean sea level, equal to +1.20 m, according to the nautical chart of Palu Bay. The bathymetry was combined with contoured topography data from BIG. The topography covers the entire domain but poorly resolves the details within Palu City, limiting the accuracy of the runup calculations within the city. Figures 1c and 5 show the topo-bathymetry of our model. The topo-bathymetry data collected prior to the earthquake do not describe localized coastal variations due to subsidence or ground failure. The tsunami propagation model includes bottom friction modeled with Manning's formula and utilizing a Manning coefficient of 0.03 (Bricker et al., 2015). We assume a still water level equal to the tide at the time of the tsunami, near high-tide (section 2). Thus, we begin the simulations with sea level offset by 1.02 m relative to the mean sea level. The COMCOT model is capable of simulating the runup of the tsunami waves by utilizing a moving boundary scheme (Wang, 2009). The simulations are carried out for the 12 hypothetical fault models from the InSAR source inversions, as well as the published slip inversion results from the USGS and Socquet et al. (2019) (presented in Figure S18).

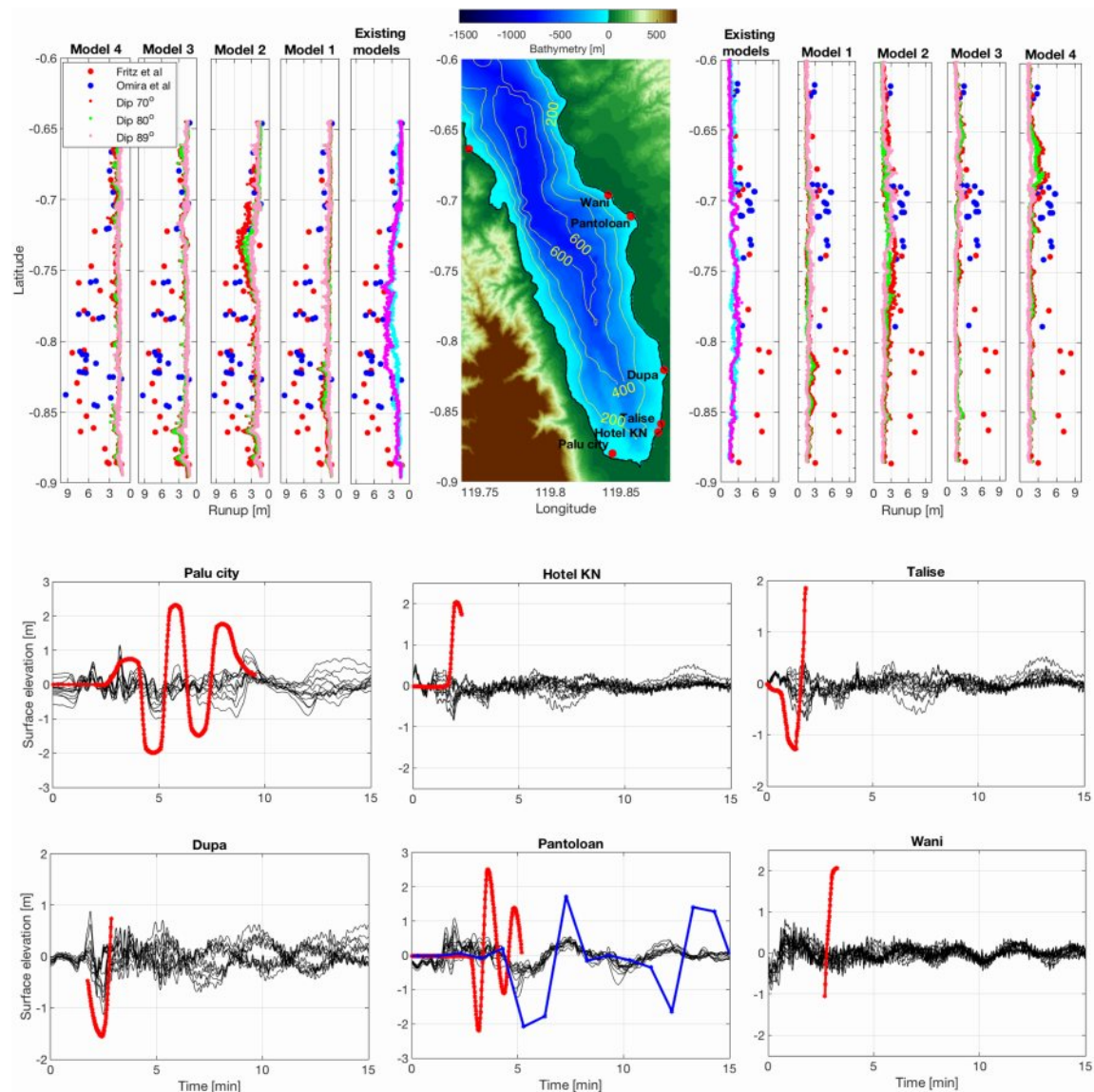


**Figure 5.** Top panels: simulated tsunami runup heights associated with the 12 earthquake models and observations from the post-tsunami surveys of Fritz et al. (2018) (large red dots) and Omira et al. (2019) (large blue dots), in meters above sea level, including the tide. The bathymetry is shown in the central panel. The yellow depth contours are expressed in meters. The runup values associated with the USGS model and Socquet et al. (2019) earthquake models are also presented as cyan and magenta curves, respectively. We have added a tidal level of 1.02 m above mean sea level to the de-tided runup values of Omira et al. (2019). Bottom panels: comparison of the video-derived tsunami time histories (red) from Carvajal et al. (2019) and the 12 tsunami simulations (black curves) with tides removed. The blue curve for Pantoloan corresponds to the tide gauge record. All curves, simulated and observed, have been de-tided, so that values can be compared.

The slip inversion of Model 1 has a similar fault geometry as the USGS and Socquet et al. (2019) model. The initial surface elevations (seen in top row of Figure 5) tend to be largest at locations further south in the bay than the USGS and Socquet models. This leads to a shift of the maximum runup toward the south; however, the maximum runup values are similar, and none of these models produces the order of magnitude runup necessary to fit the data.

### 3.3. Comparison of Simulated Tsunamis with Observations

#### 3.3.1. Maximum Elevation and Tsunami Runup

The resulting simulations of runup heights, defined as the highest elevation on land reached during the inundation process, are compared with observations at different locations in the bay. The top left and right panels of Figure 5 show the simulated tsunami runup heights along the west and east coast of Palu Bay. The large red and blue dots indicate values reported by the post-tsunami surveys conducted weeks after the

event. As a reference, the cyan and magenta dots show the simulated runup heights corresponding to the earthquake slip models of the USGS and Socquet et al. (2019), respectively. Figure S17 presents the simulated maximum tsunami elevation within Palu Bay.

None of the simulated tsunami runup heights from the 12 fault models can explain the observed values, which exceed 10 m in some locations. Model 2 with dip  $70^\circ$  (black dots), which has the largest vertical component of slip, produces runups comparable to those observed on the west coast north of  $-0.75^\circ\text{N}$ . However, the simulations are all well below the observed runup heights in the rest of the bay.

Measuring runup heights in post-tsunami surveys is challenging because the measurements commonly rely on debris lines transported during the inundation process and are obtained several days after the tsunami. The spatial distribution of runup heights is also very dependent on the small scale features of the topography and land use. The numerical simulation of runup heights is limited by the accuracy of the topography and the knowledge of coastal infrastructure including buildings and streets. In most of the numerical models, including COMCOT, these effects are ignored. The simulation of the runup might also be affected by significant uncertainties because the physics is not well resolved there by the shallow wave theory. However, large scale variations of the runup, such as the large-scale variation along the coastline of the bay (e.g., highest values at the southern end of Palu Bay), will be captured by the nonlinear shallow water wave equations (e.g., Nicolsky et al., 2011; Synolakis et al., 2008). Hence, we interpret only the large scale runup variations along the East and West coasts, when assessing the hypothetical tsunami sources.

### 3.3.2. Temporal Evolution of the Tsunami

The tsunami simulations are also compared with the tide gauge at Pantoloan and the video-derived time histories from Carvajal et al. (2019) in the lower panels of Figure 5. The video-derived time histories at Palu City, hotel KN, Talise, Dupa, Pantoloan port, and Wani are shown as red curves, with locations shown in the center top panel and given in Table 2. The video-derived time histories are provided with a time step of 1 s and are referenced to the beginning of the ground shaking observed in the videos. The beginning of the ground shaking and the earthquake origin time differ by the time required by seismic waves to travel from the fault rupture to the observation sites near Palu Bay, which is at a distance of  $\sim 64$  km from the epicenter. Carvajal et al. (2019) estimated the maximum in the temporal lag to be on the order of 10 s, which is small compared to the travel times and periods of the tsunami and, therefore, will not affect our comparison.

The black curves represent the simulated tsunami elevation from the 12 coseismic slip models. The simulated waveforms are extracted at locations that are close to the coast and are expected to represent the tsunami response at the same locations as those of the videos used to build the time histories (Table 2). In section 5 we assess the sensitivity of our results to the accuracy of the locations. Our results show that none of the simulated tsunami time histories agrees with the observed tsunami response, in magnitude or time. The comparisons of the runup heights and tsunami time series demonstrate conclusively that the coseismic deformation is insufficient to generate the observed tsunami.

The Pantoloan tide gauge record (blue) has a sample every minute, which is an average of measurements over 30 s (section 2). The video footage of the tsunami at several locations including Pantoloan port, on the other hand, shows tsunami wave periods of  $\sim 100$  s within the bay (Carvajal et al., 2019). Thus, it is likely that the tide gauge did not capture the higher frequency tsunami waves completely. The video-derived time history at Pantoloan port also provides evidence that tsunami waves arrived earlier than indicated by the tide gauge, which appears to have only captured the longer period components of the tsunami. Time-averaged tide gauge records may also have apparent periods and phases which deviate from that of the instantaneous tsunami elevation when there are higher frequency waves present. The Pantoloan video-derived and tide gauge time histories in Figure 5, for instance, present different periods and phases between times 2–5 min. See further discussion in the supporting information and Figure S1d. These are critical issues for the applicability of tide gauge stations for monitoring short period local tsunamis and demonstrates that the Pantoloan tide gauge record cannot solely be used to model and test tsunami source hypotheses for the Palu event.

## 4. Landslide Tsunami Model

The second hypothesis for the Palu event is that landslides along the coast generated the tsunami waves. The validation of this hypothesis is challenging given that the only direct tsunami record is the Pantoloan tide gauge, which did not capture the short period tsunami wave arrivals. Here we exploit the video footage analyzed by Carvajal et al. (2019) to identify potential landslide sources and then use the video-derived time

**Table 1**  
*Possible Landslide Source Locations Used in the Inversion*

Tsunami sources	Lon. (°)	Lat. (°)	Orientation (angle from W-E)
A	119.801	−0.631	180°
B	119.816	−0.694	140°
C	119.839	−0.711	140°
D	119.841	−0.734	180°
E	119.858	−0.797	140°
F	119.869	−0.855	180°
G–H	119.863	−0.875	270°
I	119.832	−0.843	−20°
J	119.824	−0.832	0°
K	119.818	−0.803	−20°
L	119.802	−0.771	−20°
M	119.796	−0.753	−20°
N	119.755	−0.662	−40°
O	119.770	−0.680	−20°

*Note.* The fourth column indicates the orientation of the landslide (i.e., perpendicular to the coast).

histories and post-tsunami surveys to determine the degree to which these slides may have been responsible for contributing to the tsunami. It is important to mention that some video-derived time histories are long and capture two to three wave periods. Other time histories, though, only partially capture the first wave (i.e., KN hotel, Talise, Dupa, and Wani). These short time histories are critical for the tsunami source inversion because they constrain the arrival time, source location, and polarity of the leading wave for the possible range of tsunami sources that fit the general features of the runup height data set.

Changes in the coastline determined from satellite imagery taken before and after the earthquake (Carvajal et al., 2019), regardless of spatial extent, were used to identify potential landslide source zones. These are indicated as zones *A* – *N* in Table 1 and Figure 6. Post-tsunami surveys also identified an additional zone *O* (Omira et al., 2019; Sassa & Takagawa, 2019). Takagi et al. (2019) conducted a bathymetric survey at zone *I* and measured a landslide of  $\sim 1$  km<sup>2</sup>. Zone *G* – *H*, *J*, and *M* are associated with more than one adjacent landslide, as shown by Carvajal et al. (2019) and Omira et al. (2019). Videos captured images of what appear to be instantaneous tsunamis generated by landslides at zones *B*, *C*, *D*, *I*, *J*, *K*, *M*, and *L* (left and right panels in Figure 6). While the video at zone *E* did not show clear evidence to confirm a source, the tsunami waves struck the coast as early as those seen in the area of zones *B*, *C*, and *D*, indicating a potentially distinct source. It is not possible to determine depth or size of the landslide sources or their generated tsunamis visually from the videos.

Laboratory experiments for simplified shallow submarine landslides showed that runup heights just landward of the landslide are as much as  $\sim 10\%$  of the width of the landslide, but the runup is significantly reduced with the landslide submergence (Liu et al., 2005). At Palu Bay, post-tsunami surveys did not measure larger runup heights just landward of the observed landslide (see Figure 5), indicating that submarine landslides occurred in deeper areas on the subsurface slope. Further evidence of deep submarine landslides is provided by the witness recording the video at zones *I*, *J*, and *K*, who survived the tsunami in a small boat. The time and duration of the landslides is not clear from the videos, apart from showing that they occurred after the earthquake. A video from a plane that took off shortly after the earthquake (bottom panel of Figure 6) shows that landslides continued to be generated as much as 100 s after the earthquake (Omira et al., 2019; Takagi et al., 2019). Given this uncertainty, we develop an inversion approach that allows for landslide source start time and duration to vary and use the unique video-derived time histories to solve for the tsunami initial surface elevations at the possible locations of these landslide tsunami sources. We varied the landslide depth in the source inversions to assess the sensitivity to that uncertainty.



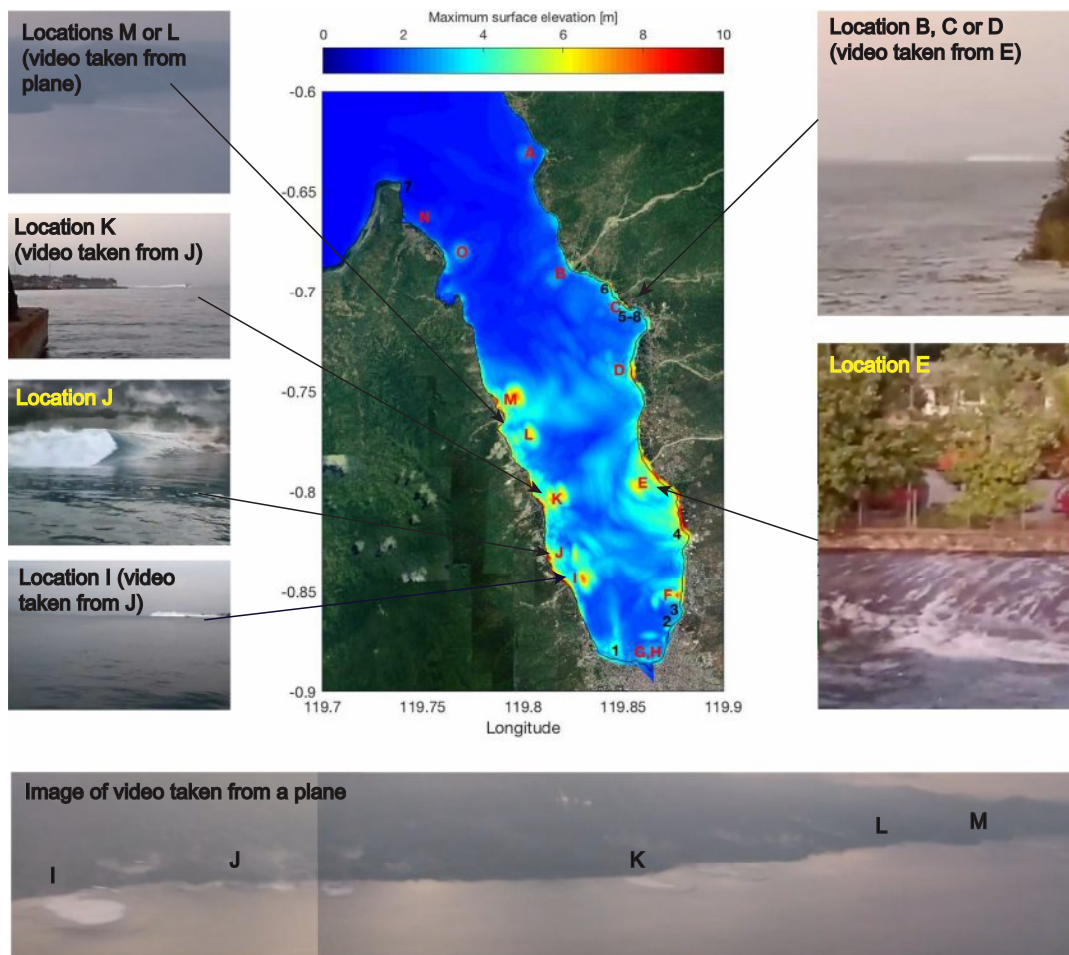


**Figure 6.** Landslide sources locations used for the tsunami inversion. Central panel: Fifteen landslide zones named A–O have been identified from existing studies. The color map represents the simulated maximum tsunami surface elevation in the 30 min following the earthquake using the results of the preferred tsunami source inversion. The locations of the tsunami time histories constraining the source inversion are indicated by black numbers and are listed in Table 2. Right and left panels: images from video footage showing the initiation of tsunami waves along the bay, apparently due to submarine landslides. Bottom: An extraordinary view of tsunami initiation was recorded from a plane at locations I, J, K, L, and M (see attribution of videos in Carvajal et al., 2019).

#### 4.1. Inversion for the Initial Elevation at the Tsunami Sources

We carry out a tsunami source inversion allowing sources at the 15 zones shown in Figure 6 (locations A–O). Each source is parameterized as a pair of Gaussian shapes to allow spatial and temporal variability in the sign of the tsunami genesis. Gaussian shapes avoid generating spurious high frequency waves, which cannot be properly simulated by the tsunami propagation model, and have been used in other tsunami source inversions (Mulia & Asano, 2016). Sources are allowed every 20 s from each zone over a duration of 100 s after the earthquake (i.e., six time steps). The selected time step is small compared to the arrival times and periods observed in the bay and is comparable to the characteristic time of some landslides recorded in the videos (e.g., video 39 on the west coast and 31 on the east coast in Carvajal et al., 2019).

The unknown parameters in the inversion are the amplitude of the Gaussian shapes. Several simplifications are adopted. First, wave nonlinearity is neglected although it may be relevant in shallow water areas. The effect of nonlinearity is assessed with a nonlinear forward simulation after finding the source amplitudes. Second, tsunami waves may have sufficiently short periods to be affected by frequency dispersion, which is neglected. We reduce the effect of dispersion by specifying sufficiently wide sources of  $\sim 1$  km. Third, the propagation of tsunamis close to the source is not expected to be well resolved by our model, as flow is commonly turbulent (Liu et al., 2005). However, it is the volume of the landslide, rather than its exact shape, that has the strongest effect on leading waves in the far field (Lo, 2018). The inversion, therefore, is designed

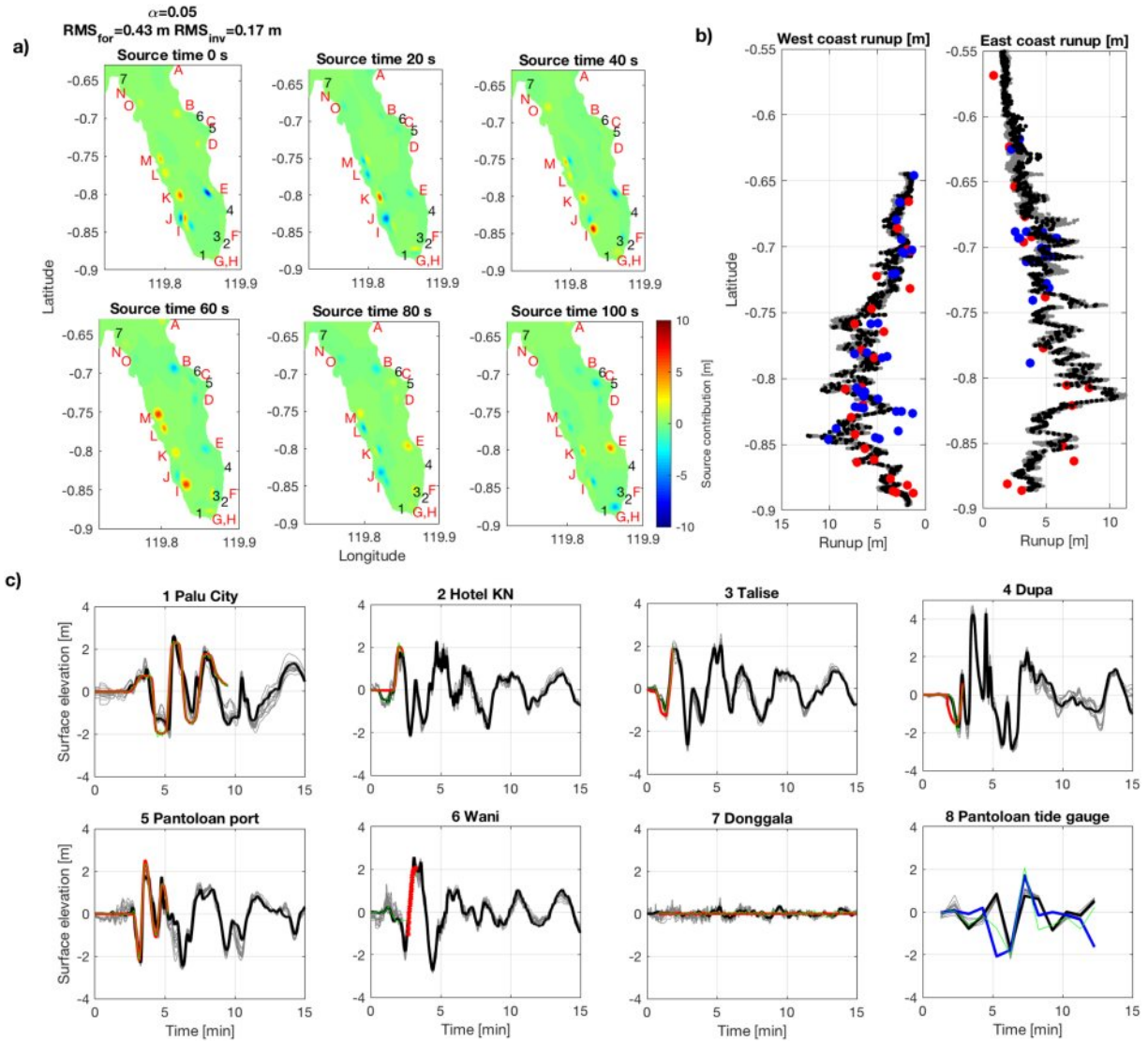


**Figure 7.** (a) Results of the landslide-generated tsunami source inversion for sources initiating at times 0, 20, 40, 60, 80, and 100 s. The propagating waves from the source are linearly superposed with the propagating waves from previous time steps. The letters indicate the source locations, and the numbers indicate the locations of the recorded tsunami time histories used to constrain the inversion (presented in c). Location 8 is the same as 5. The errors and regularization of the inverted results are shown in the top left corner. (b) Comparison of runup measurements (blue dots, Omira et al., 2019; red dots, Fritz et al., 2018), and the forward model using the resulting landslide sources (black dots). The forward models which include the combined landslide sources and coseismic deformation contribution of the 12 earthquake models are shown as gray dots, nearly indistinguishable on this scale. (c) Comparison of the video-derived time histories (red curves) and the tide gauge (blue curves), the inversion results (green curves), the forward model with landslide sources (black curves), and forward models with landslide sources combined with the coseismic contribution from the 12 earthquake models (gray curves). All time histories have been de-tided.

to estimate the large temporal and spatial scale properties of the tsunami sources but is not expected to resolve small scale source properties.

The expression for the initial tsunami surface elevation of the  $n$ th source is given by

$$G_{(x,y,n)} = \frac{1,000}{2\pi\sigma_{n,y}\sigma_{n,x}} \exp\left(\frac{-(x-x_n)^2}{2\sigma_{n,x}^2} + \frac{-(y-y_n)^2}{2\sigma_{n,y}^2}\right), \quad (5)$$

where  $x$  and  $y$  are the coordinates perpendicular and parallel to the coast, respectively,  $\sigma_{n,x}$  and  $\sigma_{n,y}$  define the across-shore and along-shore dimensions in meters of the Gaussian pulse approximating the landslide (i.e., the width and length of the source), respectively, and  $(x_n, y_n)$  is the centroid of the source. The source function in equation (5) is scaled by  $1,000$  m<sup>3</sup>, so the initial surface elevation is  $O(1$  m) at the center of each source and the total perturbed volume of each unitarian source (i.e., integrating  $G_{(x,y,n)}$  over all space) is

**Table 2***Location of the Tsunami Surface Elevation Time Histories Used in the Tsunami Source Inversion*

Time history at	Lon. (°)	Lat. (°)	Data source
Palu City	119.8442	−0.8802	Video
KN hotel	119.8766	−0.8648	Video
Talise	119.8786	−0.8590	Video
Dupa	119.8808	−0.8205	Video
Pantoloan	119.8571	−0.7117	Video, tide gauge
Wani	119.8412	−0.6966	Video
Tanjung Karang	119.7405	−0.6474	Post-tsunami survey

*Note.* The fourth column indicates the data source used to infer the time history.

1,000 m<sup>3</sup>. The pair of sources for each landslide location are separated by  $2\sigma_{n,x}$  and oriented perpendicular to the coast. The distance of the landslide to the coast is controlled by the centroid location ( $x_n, y_n$ ) and has to be specified. For the generation of the Green functions, relating the amplitude of the Gaussian sources to the tsunami response, we use the linear shallow water equations of the tsunami model COMCOT and the topo-bathymetry grid of the previous section. The unit sources (i.e., Gaussian shapes with a perturbation of 1,000 m<sup>3</sup>) are specified as an initial surface elevation at time zero to generate the Green functions. The Green functions associated with the sources at times 20, 40, 60, 80, and 100 s are simply generated by applying a temporal shift to the zero-time Green functions.

In total, the inversion solves for 14 (locations)  $\times$  2 (Gaussians per location)  $\times$  6 (times) = 168 unknown Gaussian amplitudes. The distance of the submarine landslide from the coast was varied between 0 and 1.4 km to determine that a distance of 1 km produces the simulated runups that are closest to the measurements.  $\sigma_{n,x}$  and  $\sigma_{n,y}$  were specified as 250 and 500 m, respectively, to produce sources at each zone covering an area of  $\sim 1$  km<sup>2</sup>. This size is consistent with the approximate horizontal dimensions of the landslide measured by Takagi et al. (2019) in zone I and the dimension of the coastal retreat analyzed in Carvajal et al. (2019) (Figure S8). The tsunami sources could have been distributed over depth, but we assume the equivalent total source can be concentrated at this location. Further sensitivity analyses were performed by varying the size and coastal distance showing that the locations of dominant sources are preserved, although the misfit to the data increased. In addition to the video-derived time histories, we include the tide gauge record at Pantoloan in the inversion. The tsunami inversion cannot use the Pantoloan record directly as it would suppressed source characteristics linked to the short period waves. The 30-s averaging of the tide gauge measurements constitutes a linear operator, and the record can be included in the inversion by 30-s averaging the Green functions (see eighth station in Figure 7c). We also specify a zero-elevation time history at Tanjung Karang (seventh station in Figure 7c), where the tsunami was negligible (Omira et al., 2019), and add a zero elevation during the first 2 min of the Dupa time history, before the tsunami arrival. For the tsunami source inversion we also use equation (3). For this case,  $B$  is the tsunami Green functions,  $d$  is the tsunami data of Table 2, and  $u$  are the inverted coefficients equal to the Gaussian amplitudes. We apply a Tikhonov regularization to the inversion (see equation (3)) with regularization parameter  $\alpha = 0.05$  and find the minimum source size satisfying the observations.

#### 4.2. Forward Simulation of Landslide Generated Tsunamis

The inverted Gaussian amplitudes are then employed to run a forward tsunami simulation in COMCOT using the full nonlinear shallow water equations with bottom friction. The tsunami sources are introduced at the specified times using the landslide/transient-motion forcing option of COMCOT and a .xyt format file (Wang, 2009). The central top panel of Figure 6 shows the maximum tsunami elevation over the first 30 min. Only a few sources,  $B, E, I, J, K, L$ , and  $M$ , have large amplitudes, and therefore, they constitute the main sources. The resulting sources in Figure 7a contribute over several time steps within the 100 s window, suggesting a long-duration process. Landslides triggered after earthquake ground shaking have been observed over extended durations and analyzed for other events (Keefer, 2002). The propagating waves from the sources are linearly superposed with the propagating waves from the previous time steps. Some

secondary sources, *B*, *F*, *G*, *H*, *J*, and *O*, with smaller amplitudes are also estimated for one or two time steps within the 100 s generation.

#### 4.3. Comparison of Simulated Tsunamis with Observations

Figure 7c shows the video-derived time histories (red curves) and the forward tsunami simulation (black curves). The linearized solution (green) only extends the length of the video-derived waveforms, whereas the tide gauge data are fitted over the entire 15 min. However, the nonlinear forward model waveforms are shown at all sites for the entire 15 min and are used to calculate the simulated runup values. Over the available time period for comparison, the linearized solution does not deviate from the nonlinear forward model simulation, showing wave nonlinearity does not significantly affect the results. The RMS error of the forward model waveforms with respect to the video-derived time histories is 0.43 m, about 10% of the typical wave heights for most of the observation locations. The fit of the model to the tide gauge at Pantoloan port record (blue curve) has the largest differences; however, the model captures the long period features occurring 5 min after the earthquake (see the black and gray curves in the fifth and eighth stations of Figure 7c). By modeling the full spectral content of the tsunami waves and applying the approximate filter to the simulated time series to compare to the tide gauge record, we have been able to exploit both data sets and find a simulation that fits both to an acceptable level.

Forward simulations can be qualitatively compared with other observational evidence when time history data are absent. The video-derived time history at Wani, for instance, starts  $\sim 3$  min after the earthquake. The forward simulated waveform before that time, on the other hand, predicts a significant leading trough. Witnesses at Wani indicated that a large leading trough was observed before the largest tsunami wave (Omira et al., 2019), consistent with the simulation, even though the size of that trough is unknown. In Dupa, the videos only recorded the initial drawdown of the tsunami when it arrived at the coast. The simulation shows that after the observation interval, a larger wave with positive amplitude struck the coast. Satellite imagery at that location (Carvajal et al., 2019) shows traces of a large inundation there. The spatial distribution of the simulated runup from the forward model agrees very well with the runup measured in post-tsunami surveys, as seen by the black dots in Figure 7b. The values fall within the scatter of the observed runup values, as opposed to the simulated runups from the coseismic models shown in Figure 5. As described in section 3.3.1 and illustrated by the differences in the two post-tsunami surveys of runup heights (red and blue dots), there is considerable variability of the observations due to the dependence of runup on small scale topography, surface properties, and land use. For this reason, we compare the model results to both runup data sets when calculating the RMS misfit, to accommodate this uncertainty. Runup data were not used in the inversion but were used as a reference to find the best fitting model in terms of the source widths and distance to the coast (see quantitative RMS values in the sensitivity analyses shown in Figure S22).

The black waveforms in Figure 7c showing the landslide simulations do not contain any contribution from coseismic deformation. To appreciate the relative contributions of landslides versus coseismic deformation in generating the tsunami, we carry out simulations combining the two types of sources for each of the 12 earthquake slip models. The gray dots and in Figure 7b and the gray lines in Figure 7c correspond to simulations with the combined effects. The coseismic contribution to the tsunami is small and provides little variation to the landslide-only waveforms. Conclusively, the landslide sources alone are sufficient to explain the tsunami. Also notable is that the largest landslide sources are found between latitudes  $-0.86^\circ$  and  $-0.75^\circ$  (top central panel in Figure 6) where the slip is largest in the retrieved finite fault static slip inversions (Figure 3b and supporting information figures). This suggests that the landslide-generated tsunami runup has a similar N-S variation along the coast to that of the earthquake source because strong ground motion focused near the location of the maximum slip was strong enough to generate larger landslides. That N-S variation of the runup may be controlled by the bathymetry and the earthquake location and is thus similar for the two types of source. However, the amplitude is controlled by the relative sizes of the two types of source and is much greater for the landslides.

### 5. Stability of Tsunami Source Inversion

As pointed out by Carvajal et al. (2019), the time histories reconstructed from video footage contain errors describing the actual tsunami response. While the period estimation is expected to be very accurate, the absolute arrival times for videos without seismic shaking, and the tsunami amplitudes for all videos may



contain errors. Uncertainties in the observation locations and viewing angle contribute to a lesser extent to uncertainties in the inversion results. We assess the impact of these sources of uncertainty on the stability of our tsunami inversion results in section 4 by perturbing the times, amplitudes, and locations. We finally assess the sensitivity of the tsunami source inversion to the assumed values of the size and location of landslide sources. We point out that the uncertainties in the absolute timing and time history amplitudes in sections 5.1 and 5.2, respectively, affect the data vector  $d$  in equation (3) only and do not require the inverse of new matrices of Green functions. As a consequence, inversion samples can be computed rapidly, and therefore, Monte Carlo simulations can be adopted to assess the impact of uncertainties. The uncertainties of size and location in sections 5.3 and 5.4, in contrast, affect the Green function matrix  $B$  in equation (3). The construction of Green function matrices require a significant amount of time, making a Monte Carlo simulation unfeasible. Alternatively, this problem, we conduct a sensitivity analysis for the uncertainties in size and location.

### 5.1. Sensitivity to Uncertainties in the Absolute Timing of the Video-Derived Time Histories

The sensitivity of inversion results to the observation errors is investigated using a Monte Carlo-based approach. The arrival times of Palu City, Dupa, and Wani were not determined accurately because the initiation of the ground shaking was not recorded or because the videos are recorded relatively far from the coast. The video footage at Palu City, for instance, did not record the earthquake ground shaking (videos 15–20 in Carvajal et al., 2019). Carvajal et al. (2019) assumed a lapse of  $\sim 2$  min between the earthquake origin time and the initiation of the earliest videos. This assumption has large uncertainty, since the video appeared to be prompted by the approach of the tsunami rather than the earthquake shaking. In this study, we assume that the estimated arrival time has an uncertainty of  $\pm 30$  s. The video footage at Dupa (video 14 in Carvajal et al., 2019) also missed the earthquake ground shaking. However, in this case the video appeared to be initiated right after the end of the earthquake, as the video was apparently prompted by the earthquake ground shaking rather than the approach of tsunami waves, as people seem to be evacuating their homes and were not aware of the tsunami when they started recording. Thus, we assume that the arrival time has an uncertainty of  $\pm 15$  s from that reported by Carvajal et al. (2019). The video footage at Wani (videos 7–8 in Carvajal et al., 2019) recorded the earthquake and the tsunami continuously. However, the CCTV cameras recording earthquake and tsunami were located on land  $\sim 150$  m from the shoreline. The travel time of the inundation over that distance is unknown and constitutes a source of uncertainty in the estimation of arrival times at the shore. Carvajal et al. (2019) estimated a tsunami travel time from the shoreline to the CCTV cameras of 30 s. Here we assume an uncertainty of  $\pm 15$  s in the estimated arrival time. It is noteworthy that the CCTV cameras captured a power outage  $\sim 18$  s before the tsunami arrival. The timing may suggest that the power outage was due to the tsunami striking electric lines between the shoreline and the CCTV cameras.

There is a possibility that a significant error in the arrival time captured by some of the video recordings could displace the locations of the retrieved sources shown in Figure 7a. To test this, we create 50 realizations with randomly translated time histories in Palu City, Dupa, and Wani only. The arrival time uncertainties are modeled here as a random value which perturbs the start of the time history. The uncertainty is specified as a zero mean uniform distributed random value whose standard deviations are given by our estimated uncertainties. We invert the perturbed time histories to find the landslide contribution to water elevation at each 20 s source time step. Then at each source time, we obtained the mean of the 50 spatial maps of water surface elevation to produce a map of the mean tsunami source and the standard deviation at that time. The first column of Figure 8 shows the mean tsunami source water elevation at each source time, and the second column shows the standard deviation. Note that the mean source amplitudes and locations are similar to those of the preferred model. The standard deviation is smaller than 50% for most of the sources. Despite there are some sources with high standard deviation, they are located where the largest sources are, indicating it is unlikely the source inversion missed a significant tsunami source. This analysis shows that the inversion is not significantly affected by the arrival time uncertainties. Figure S21 presents quantitative calculations of the uncertainty of the model values  $u$  (see equation (3)), representing the source Gaussian amplitudes.

### 5.2. Sensitivity to Uncertainties of the Time history Amplitudes

The second experiment adds a perturbation to the amplitudes estimated by Carvajal et al. (2019). Errors in the observations may be related to the difficulty in finding a good reference for the still water level in order to measure the size of tsunami waves, for example, structures close to the coast within the video frame. Consequently, errors are described as a constant factor multiplying each time history. It is more difficult

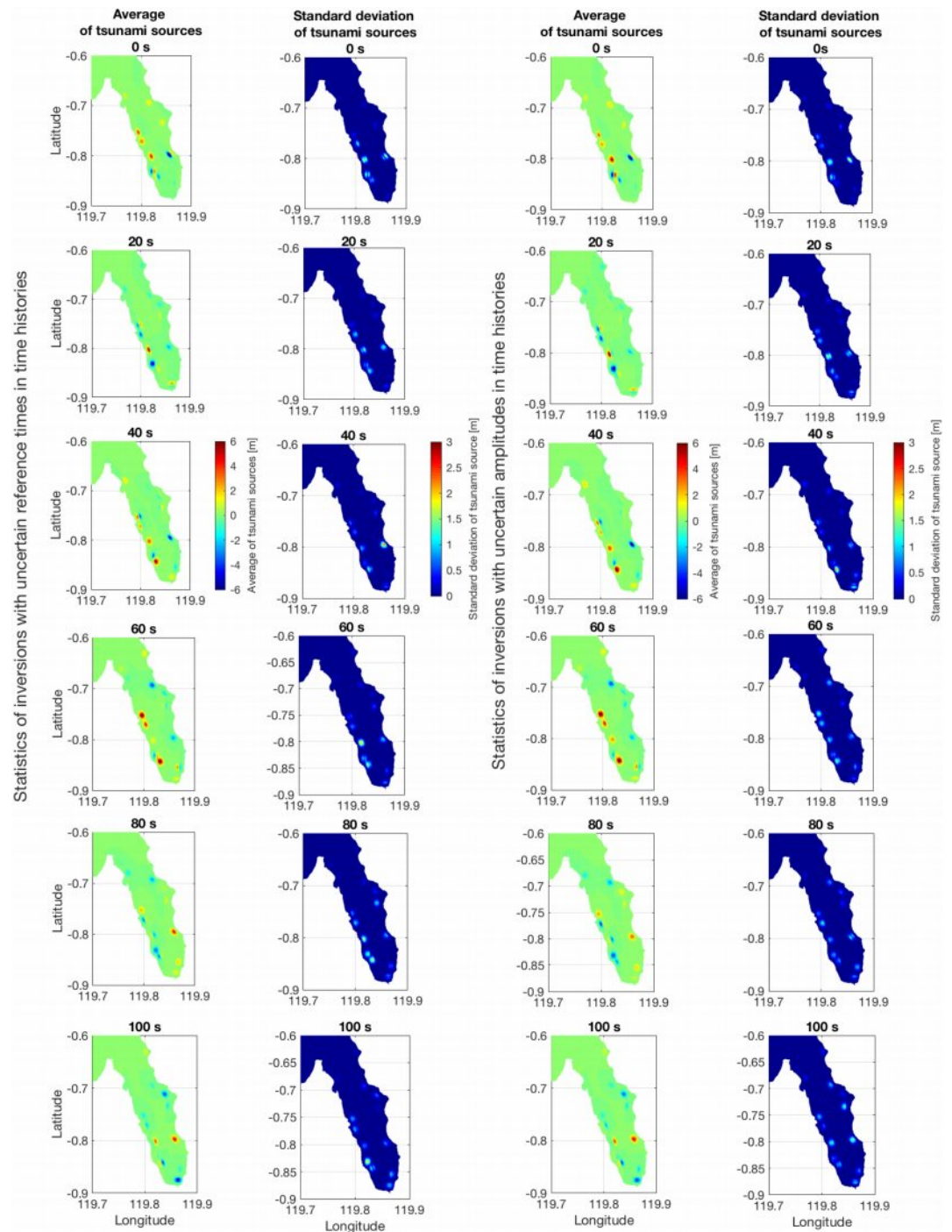


**Figure 8.** First and second columns: mean and standard deviation of the tsunami source inversion results using 50 samples of the tsunami time histories with perturbed reference times. Third and fourth columns: average and standard deviation of the tsunami source inversion results using 50 samples of the tsunami time histories with perturbed observed amplitudes.

to determine the magnitude of these errors than the uncertainties of arrival times. We arbitrarily perturb the time histories by multiplying by a random uniformly distributed factor, defined between 0.5 and 1.5. This range envelops the possible uncertainties of the amplitude estimation of Carvajal et al. (2019) and are realistic given the video-based inferences that consider the reliability with which the viewer can assess the uncertainty in the height of structures and other vertical references evaluated over the course of the entire

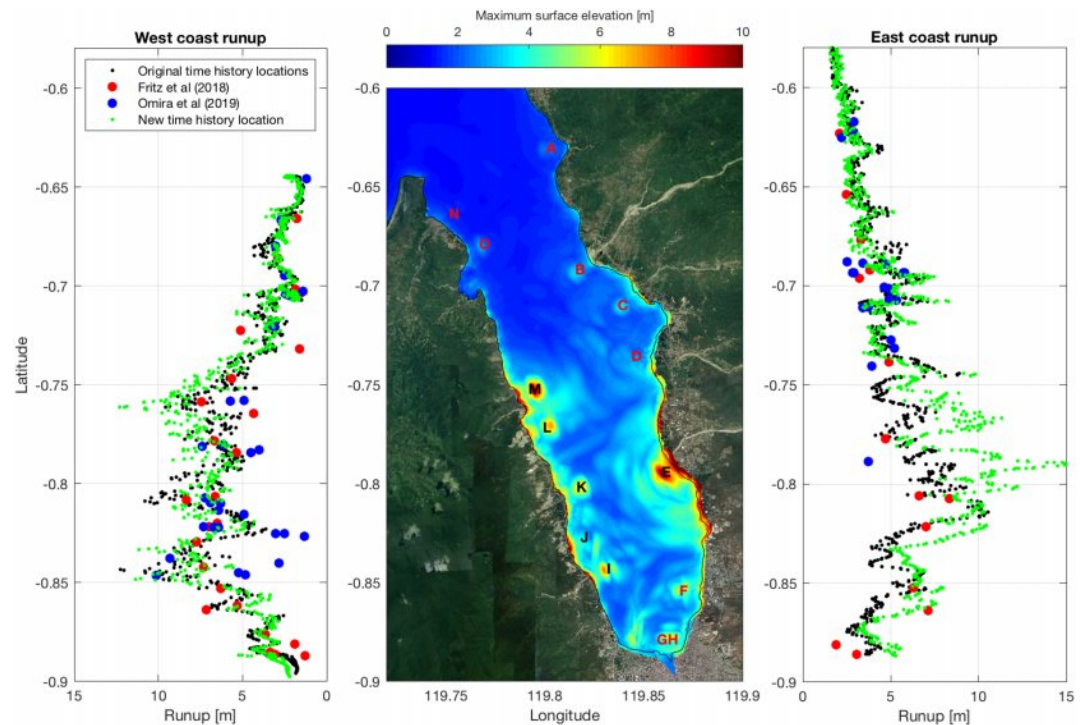


**Figure 9.** Sensitivity analysis of the inversion results to the observation locations. The left and right panels show the corresponding runup results associated with the original locations (black dots), the runup assuming locations 200 m farther from the coast (green dots) and runup measurements (red and blue dots). Central panel: maximum tsunami elevation during the first 30 min following the earthquake and using the 200 m shifted observation locations. The high water surface elevation indicates which of the sources are dominant.

video, not just at the time of the peak amplitude. We again adopt a Monte Carlo-based approach. The third and fourth columns of Figure 8 show the mean and standard deviation of the map of the modeled tsunami source water elevation at each source time based on inverting 50 realizations of time series with perturbed amplitudes. Again, we observe a small impact of this source of uncertainty on the inversion results, with standard deviations smaller than 50% of the average values. Figure S21 quantifies the uncertainties for the inversion model values  $u$ , representing the source Gaussian amplitudes.

### 5.3. Sensitivity to Uncertainties of the Time History Observation Locations

As a third experiment we analyze the sensitivity of the tsunami source inversion to the uncertainty of the time history locations. The locations of video-derived time histories are assumed to be close to the shore at mean sea level. These locations, though, are approximate, and their uncertainties may produce an impact on the inversion results. As a mean of assessing the impact of this uncertainty, we assume the simulated time histories (and Green functions) are located 200 m farther offshore from the coast than the best estimate of the locations of Table 2. The new locations are shown in Table S1 and Figure S20. We think this translation of 200 m envelops the uncertainty of the location where tsunami waves were recorded in the video footage because of the size of the field of view in the video recordings and the requirement that only videos with geolocations identified using google maps were included in the database (Carvajal et al., 2019). In this analysis we do not change the location of the time history of Pantoloan port, as that location is relatively certain, having been inferred from the time history of a ship with known location (Carvajal et al., 2019). The right and left panels of Figure 9 show a comparison of the simulated runup height with time histories at the preferred locations (black dots) and the simulated runup heights with time histories at the perturbed locations (green dots) farther offshore. Note that the simulated runup heights on the western coast have small differences. The runup heights on the eastern coast, however, have some larger differences. The central panel shows the maximum water elevation associated with the new inversion. Note that the contribution of the sources is similar to that of the preferred inversion (see central panel in Figure 6) but with greater contributions from some secondary sources (e.g., location GH). Despite this, the differences do not change the main conclusions of this section, in particular the success in modeling the video-derived time histories of

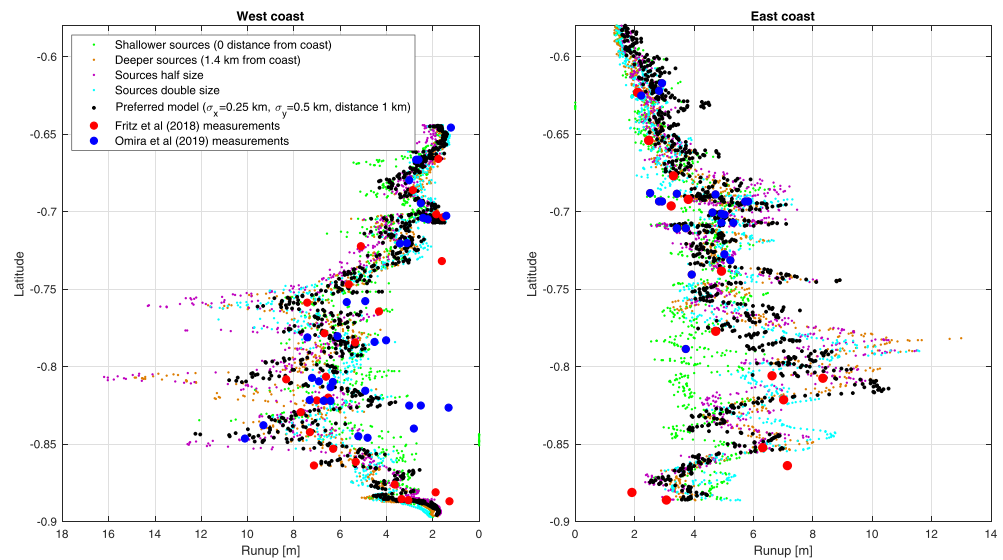


**Figure 10.** Sensitivity analysis of the size and location of the landslides with respect to the shoreline. The landslides with twice the size have values of  $\sigma_{n,x} = 0.5$  km by  $\sigma_{n,y} = 1$  km. The landslides with half the size have values of  $\sigma_{n,x} = 0.125$  km by  $\sigma_{n,y} = 0.25$  km. The shallower landslide locations are next to the coast, and the deeper landslides are located at 1.4 km from the coast. The latter approximately locates the landslides at the toe of the coastal slope.

the surface elevation with a small number of dominant landslide sources. The quantitative assessment of the results of the sensitivity analysis are shown in Figure S22a, in which we calculate the RMS errors of the simulated runup relative to observations.

#### 5.4. Sensitivity of the Tsunami Source Inversion to the Assumed Size and Locations of Landslide Sources

We conduct a sensitivity analysis in which we vary the areal extent of the landslides (being defined by  $\sigma_{n,x}$  and  $\sigma_{n,y}$ ) and their assumed location from the coast (being defined by  $(x_n, y_n)$ ) from those specified in our preferred model. The bounds for the shift in location and areal extent are based on the horizontal scale of the tsunamis in the videos at their earliest observation time. In particular the airplane video (Carvajal et al., 2019) provides a reasonable bound for the source size and maximum distance from the shore, given the observations of the tsunami waves at a time when they appear to have a circular source. Figure 10 show the simulated runup of four inversions using different areal extent and location. In general, the preferred model of section 4 (black dots) simulates the best runup heights as compared to the data.

All of the inversions predict significant sources in the same dominant locations presented for our preferred model in section 4 (see Figures S23–S26). Quantitative RMS errors of runup misfit for all inversions included in the sensitivity analysis for the range of source sizes and locations are shown in Figures S22b and S22c. Inversions that produce larger secondary sources produce simulated runup profiles that deviate significantly from those observed and are thus unreliable. The calculation of these RMS runup errors provide convincing evidence that the sensitivity study has captured the range of realistic models. Conclusively, our preferred model better predicts the runup, as compared to measurements (i.e., black dots of Figure 10).

## 6. Conclusions and Discussion

The Palu tsunami challenged the conventional assumptions and understanding of tsunami hazard related to strike-slip earthquakes. Our results show that landslides, triggered by near-source strong ground shaking from a strike-slip earthquake, have the potential to generate significantly damaging and deadly local tsunamis.

Tsunami source locations and time histories of the tsunami surface elevation were derived from crowd-sourced videos from social media and used in the present study to numerically model the Palu tsunami. Our tsunami simulations of section 3 show that coseismic sources alone cannot match all of the observations from runup heights, tide gauges, and the video-derived time histories. The video footage showed locations



where evidence of coastal landslides and subsequent tsunami waves occurred during and after the earthquake. These landslide locations provided realistic candidates for hypothetical tsunami sources, which were employed in section 4 to conduct a tsunami source inversion, constrained with video-derived time histories of the tsunami surface elevation. Our inversion results show that a few landslides from the potential candidate locations on the east and west coasts of Palu Bay provided the main tsunamigenic source contributions. These tsunamigenic sources are located south of latitude 0.7, where the maximum slip was identified in the source inversions and the maximum ground shaking likely occurred. The forward tsunami simulation associated with the inverted sources are consistent with all of the tsunami data, including surveyed runup heights.

We found that tsunamis generated by earthquake-triggered landslides may produce tsunami waves at much shorter periods than typically observed, but which can prove to be devastating. These shorter period waves are reproduced in the nonlinear forward simulations based on the landslide sources. This type of landslide source is more likely in the steep topography and bathymetry of the strike-slip coastal environment, as opposed to coastlines at greater distance from offshore thrust faults within the subduction zone. In the Palu tsunami, for instance, the video-derived time histories of the surface elevation showed tsunami waves with periods of  $\sim 100$  s that were responsible for catastrophic damage. These shorter, earlier, and largest tsunami waves were not observed by the tide gauge at Pantoloan, which was sampling at typical periods employed for operational networks. This observation has twofold implications in this event. First, tsunami modeling cannot be constrained solely and directly by the Pantoloan tide gauge record. Second, tide gauge operations should be adapted to the local tsunami characteristics if they are planned to provide data for assessing tsunami hazard in Palu Bay.

The results of this study prompt important questions to be answered for effective tsunami hazard assessment in strike-slip environments. It is possible that the high sediment load from rivers flowing into Palu Bay as a result of the rapid deformation within the Palu-Koro fault zone creates an increased susceptibility to submarine landslides. This characteristic of the coastline is likely to be an amplifying factor in any future event. The potential for future earthquakes triggering tsunamigenic landslides, such as aftershocks or rupture of unbroken fault sections, should be considered in any tsunami hazard assessment for the area. The general conclusion that landslides are a contributing factor to tsunami hazard where the geometry of the coastline is strongly linked to coastal transform faulting should be investigated more thoroughly. Regions with similar geologic and tectonic settings to those of Palu Bay have experienced tsunamis, such as Port-au-Prince in Haiti in 2010 (Hornbach et al., 2010; Sassa & Takagawa, 2019), although with much lesser direct impact. Other examples are the moderate 1810 Baja California (Ramírez-Herrera et al., 2019) and the 2016 Kaikoura (Bai et al., 2017) earthquakes, where unexpected tsunamis were generated. It is also possible that even the past historical tsunamis in the Palu-Koro fault region are related to this phenomenon. It is worthwhile to investigate the geometry of offshore structures near active coastal transform faults and consider landslide susceptibility in scenarios for tsunami simulations as part of a comprehensive hazard assessment. While our simulations suggest a secondary role of the coseismic deformation generating the tsunami in Palu Bay, shallow complexities of the fault geometry beneath water bodies have the potential to generate significant dip-slip components and tsunamis. Hence, a thorough assessment of the tectonic setting of Palu Bay and other regions is also needed.

## References

- Bai, Y., Lay, T., Cheung, K. F., & Ye, L. (2017). Two regions of seafloor deformation generated the tsunami for the 13 November 2016, Kaikoura, New Zealand earthquake. *Geophysical Research Letters*, 44, 6597–6606. <https://doi.org/10.1002/2017GL073717>
- Bao, H., Ampuero, J.-P., Meng, L., Fielding, E. J., Liang, C., Milliner, C. W. D., et al. (2019). Early and persistent supershear rupture of the 2018 magnitude 7.5 Palu earthquake. *Nature Geoscience*, 10, 200–205.
- Bellier, O., Sébrier, M., Beaudouin, T., Villeneuve, M., Braucher, R., Bourles, D., et al. (2001). High slip rate for a low seismicity along the Palu-Koro active fault in central Sulawesi (Indonesia). *Terra Nova*, 13(6), 463–470.
- Bricker, J. D., Gibson, S., Takagi, H., & Imamura, F. (2015). On the need for larger Manning's roughness coefficients in depth-integrated tsunami inundation models. *Coastal Engineering Journal*, 57(02), 1550005.
- Carvajal, M., Araya-Cornejo, C., Sepúlveda, I., Melnick, D., & Haase, J. S. (2019). Nearly instantaneous tsunamis following the  $M_W$  7.5 2018 Palu earthquake. *Geophysical Research Letters*, 46, 5117–5126. <https://doi.org/10.1029/2019GL082578>
- Chen, C. W., & Zebker, H. A. (2001). Two-dimensional phase unwrapping with use of statistical models for cost functions in nonlinear optimization. *JOSA A*, 18(2), 338–351.
- Frederik, M. C. G., Adhitama, R., Hananto, N. D., Sahabuddin, S., Irfan, M., Moefti, O., et al. (2019). First results of a bathymetric survey of Palu Bay, Central Sulawesi, Indonesia following the tsunamigenic earthquake of 28 September 2018. *Pure and Applied Geophysics*, 176(8), 3277–3290.

## Acknowledgments

This paper is dedicated to all the Palu citizens who suffered with the 2018 Palu disaster and all the citizen scientists who collected valuable information. ALOS-2 satellite data were provided by the JAXA under investigation 1148 (PI David Sandwell) and can be obtained online (<https://www.eorc.jaxa.jp/ALOS/en/index.htm>). We would like to thank the support of BIG who shared bathymetry data and tsunami records at Pantoloan and Mamuju, which are available online (<http://www.big.go.id>). BIG further provided valuable information of the Pantoloan tide gauge operation. We thank Xiaoming Wang for sharing an updated version of COMCOT (available for download at <http://shop.gns.cri.nz>) and Danny Hilman Natawidjaja for interesting discussions on the geological setting of Palu bay. We also thank Zoe Yin for useful discussions and editorial comments on this paper. I. Sepúlveda would like to thank the support of the Green Foundation. J. S. Haase acknowledges support from National Science Foundation (NSF) Grant OAC-1835372 and AGS-1642650 and NASA Grant NNX15AU19G. P. Liu would like to acknowledge the support from National Research Foundation (Singapore) through a grant to the National University of Singapore and National Science Foundation through grants to Cornell University. M. Carvajal acknowledges the support of the Iniciativa Científica Milenio (ICM) through Grant NC160025, FONDECYT Project 1190258, and the Doctoral Program of Geological Sciences of the Universidad de Concepción. We finally acknowledge the constructive comments from editors and reviewers.

- Fritz, H. M., Borrero, J. C., Synolakis, C. E., & Yoo, J. (2006). 2004 Indian Ocean tsunami flow velocity measurements from survivor videos. *Geophysical Research Letters*, 33, L24605. <https://doi.org/10.1029/2006GL026784>
- Fritz, H. M., Phillips, D. A., Okayasu, A., Shimozone, T., Liu, H., Mohammed, F., et al. (2012). The 2011 Japan tsunami current velocity measurements from survivor videos at Kesennu Bay using LiDAR. *Geophysical Research Letters*, 39, L00G23. <https://doi.org/10.1029/2011GL050686>
- Fritz, H. M., Synolakis, C., Kalligeris, N., Skanavis, V., Santoso, F., Rizal, M., Prasetya, G. S., Liu, Y., & Liu, P. L. F. (2018). Field survey of the 28 September 2018 Sulawesi tsunami (Invited). Retrieved from <https://agu.confex.com/agu/fm18/meetingapp.cgi/Paper/476809>
- Fuentes, M., Riquelme, S., Ruiz, J., & Campos, J. (2018). Implications on 1+ 1 D tsunami runup modeling due to time features of the earthquake source. *Pure and Applied Geophysics*, 175(4), 1393–1404.
- Gusman, A. R., Supendi, P., Nugraha, A. D., Power, W., Latief, H., Sunendar, H., Widiyantor, S., DaryonoWiyono, S. H., Hakim, A., Muhari, A., Wang, X., Burbidge, D., Palgunadi, K., Hamling, I., & Daryono, M. R. (2019). Source model for the tsunami inside Palu Bay following the 2018 Palu earthquake, Indonesia. *Geophysical Research Letters*, 46, 8721–8730. <https://doi.org/10.1029/2019GL082717>
- Heidarzadeh, M., Muhari, A., & Wijanarto, A. B. (2019). Insights on the source of the 28 September 2018 Sulawesi tsunami, Indonesia based on spectral analyses and numerical simulations. *Pure and Applied Geophysics*, 176(1), 25–43.
- Hornbach, M. J., Braudy, N., Briggs, R. W., Cormier, M.-H., Davis, M. B., Diebold, J. B., et al. (2010). High tsunami frequency as a result of combined strike-slip faulting and coastal landslides. *Nature Geoscience*, 3(11), 783.
- Kajiura, K. (1963). The leading wave of a tsunami. *Bulletin of the Earthquake Research Institute*, 41, 535–571.
- Keefer, D. K. (2002). Investigating landslides caused by earthquakes—A historical review. *Surveys in Geophysics*, 23(6), 473–510.
- Liu, P. L.-F., Wu, T.-R., Raichlen, F., Synolakis, C. E., & Borrero, J. C. (2005). Runup and rundown generated by three-dimensional sliding masses. *Journal of Fluid Mechanics*, 536, 107–144.
- Lo, H. Y. (2018). Modeling landslide-generated tsunamis with long-wave equations. (Unpublished doctoral dissertation).
- Lotto, G. C., Nava, G., & Dunham, E. M. (2017). Should tsunami simulations include a nonzero initial horizontal velocity? *Earth, Planets and Space*, 69(1), 117.
- Lynett, P. J., Borrero, J. C., Weiss, R., Son, S., Greer, D., & Renteria, W. (2012). Observations and modeling of tsunami-induced currents in ports and harbors. *Earth and Planetary Science Letters*, 327, 68–74.
- Mai, P. M. (2019). Supershear tsunami disaster. *Nature Geoscience*, 12(3), 150–151.
- Muhari, A., Imamura, F., Arikawa, T., Hakim, A., & Afriyanto, B. (2018). Solving the puzzle of the September 2018 Palu, Indonesia, tsunami mystery: Clues from the tsunami waveform and the initial field survey data. *Journal of Disaster Research*, 13, sc20181108.
- Mulia, I. E., & Asano, T. (2016). Initial tsunami source estimation by inversion with an intelligent selection of model parameters and time delays. *Journal of Geophysical Research: Oceans*, 121, 441–456. <https://doi.org/10.1002/2015JC010877>
- Nicolsky, D. J., Suleimani, E. N., & Hansen, R. A. (2011). Validation and verification of a numerical model for tsunami propagation and runup. *Pure and Applied Geophysics*, 168(6-7), 1199–1222.
- Okada, Y. (1985). Surface deformation due to shear and tensile faults in a half-space. *Bulletin of the seismological society of America*, 75(4), 1135–1154.
- Omira, R., Dogan, G. G., Hidayat, R., Husrin, S., Prasetya, G., Annunziato, A., et al. (2019). The September 28th, 2018, tsunami in Palu-Sulawesi, Indonesia: A post-event field survey. *Pure and Applied Geophysics*, 176, 1379–1395.
- Pawlowicz, R., Beardsley, B., & Lentz, S. (2002). Classical tidal harmonic analysis including error estimates in MATLAB using T\_TIDE. *Computers & Geosciences*, 28(8), 929–937.
- Pelinovsky, E., Yuliadi, D., Prasetya, G., & Hidayat, R. (1997). The 1996 Sulawesi tsunami. *Natural Hazards*, 16(1), 29–38.
- Prasetya, G., De Lange, W., & Healy, T. (2001). The Makassar strait tsunamigenic region, Indonesia. *Natural Hazards*, 24(3), 295–307.
- Ramirez-Herrera, M. T., Corona, N., & Castillo-Aja, R. (2019). Revealing the source of the 27 August 1810 Loreto, Baja California, tsunami from historical evidence and numerical modelling. *Pure and Applied Geophysics*, 176(7), 2951–2967.
- Sandwell, D., Mellors, R., Tong, X., Wei, M., & Wessel, P. (2011). GMTSAR: An InSAR processing system based on generic mapping tools.
- Sassa, S., & Takagawa, T. (2019). Liquefied gravity flow-induced tsunami: First evidence and comparison from the 2018 Indonesia Sulawesi earthquake and tsunami disasters. *Landslides*, 16(1), 195–200.
- Simons, M., Fialko, Y., & Rivera, L. (2002). Coseismic deformation from the 1999  $M_W$  7.1 Hector Mine, California, earthquake as inferred from InSAR and GPS observations. *Bulletin of the Seismological Society of America*, 92(4), 1390–1402.
- Socquet, A., Hollingsworth, J., Pathier, E., & Bouchon, M. (2019). Evidence of supershear during the 2018 magnitude 7.5 Palu earthquake from space geodesy. *Nature Geoscience*, 12(3), 192–199.
- Socquet, A., Simons, W., Vigny, C., McCaffrey, R., Subarya, C., Sarsito, D., et al. (2006). Microblock rotations and fault coupling in SE Asia triple junction (Sulawesi, Indonesia) from GPS and earthquake slip vector data. *Journal of Geophysical Research*, 111, B08409. <https://doi.org/10.1029/2005JB003963>
- Song, Y. T., Fu, L.-L., Zlotnicki, V., Ji, C., Hjørleifsdottir, V., Shum, C. K., & Yi, Y. (2008). The role of horizontal impulses of the faulting continental slope in generating the 26 December 2004 tsunami. *Ocean Modelling*, 20(4), 362–379.
- Song, Y. T., Mohtat, A., & Yim, S. C. (2017). New insights on tsunami genesis and energy source. *Journal of Geophysical Research: Oceans*, 122, 4238–4256. <https://doi.org/10.1002/2016JC012556>
- Synolakis, C. E., Bernard, E. N., Titov, V. V., Kanoğlu, U., & Gonzalez, F. I. (2008). Validation and verification of tsunami numerical models. *Tsunami science four years after the 2004 indian ocean tsunami* (pp. 2197–2228). Birkhäuser Basel Springer.
- Takagi, H., Pratama, M. B., Kurobe, S., Esteban, M., Aránguiz, R., & Ke, B. (2019). Analysis of generation and arrival time of landslide tsunami to Palu City due to the 2018 Sulawesi earthquake. *Landslides*, 16, 983–991.
- Tanioka, Y., & Satake, K. (1996). Tsunami generation by horizontal displacement of ocean bottom. *Geophysical Research Letters*, 23, 861–864.
- Ulrich, T., Vater, S., Madden, E. H., Behrens, J., van Dinther, Y., van Zest, I., et al. (2019). Coupled, physics-based modeling reveals earthquake displacements are critical to the 2018 Palu, Sulawesi tsunami. *Pure and Applied Geophysics*, 176, 4069–4109. <https://doi.org/10.1007/s00024-019-02290-5>
- Wang, X. (2009). User manual for COMCOT version 1.7 (first draft). Cornell University.
- Watkinson, I. M., & Hall, R. (2017). Fault systems of the eastern Indonesian triple junction: Evaluation of quaternary activity and implications for seismic hazards. *Geological Society, London, Special Publications*, 441(1), 71–120.
- Wessel, P., Smith, W. H., Scharroo, R., Luis, J., & Wobbe, F. (2013). Generic mapping tools: Improved version released. *Eos, Transactions American Geophysical Union*, 94(45), 409–410.
- Yolsal-Çevikbilen, S., & Taymaz, T. (2019). Source characteristics of the 28 September 2018  $M_W$  7.5 Palu-Sulawesi, Indonesia (SE Asia) earthquake based on inversion of teleseismic bodywaves. *Pure and Applied Geophysics*, 176(10), 4111–4126.